Triple iron isotope constraints on the role of ocean iron sinks in early atmospheric oxygenation

Triple Iron Isotope Constraints on the Role of Ocean Iron Sinks in Early Atmospheric Oxygenation

Andy W. Heard[1*], Nicolas Dauphas[1], Romain Guilbaud[2], Olivier J. Rouxel[3], Ian B. Butler[4], Nicole X. Nie[1,5], Andrey Bekker[6,7]

[1]Origins Laboratory, Department of the Geophysical Sciences and Enrico Fermi Institute, The University of Chicago, 5734 South Ellis Avenue, Chicago, IL 60637, USA.
[2]Géosciences Environnement Toulouse, CNRS, UMR5563, 14 Avenue Edouard Belin, 31400 Toulouse, France.
[3]Unité Géosciences Marines, IFREMER, Plouzané 29280, France.
[4]School of Geosciences, University of Edinburgh, Grant Institute, Edinburgh EH9 3JW, UK.
[5]Earth and Planets Laboratory, Carnegie Institution for Science, Washington, DC 20015, USA.
[6]Department of Earth and Planetary Sciences, University of California, Riverside, CA 92521, USA.
[7]Department of Geology, University of Johannesburg, Johannesburg 2006, South Africa.
*e-mail: andyheard@uchicago.edu

Submitted to Science
July 28th, 2020
2594 words, 3 figures

Abstract (113 words)

The role that iron played in the oxygenation of Earth's surface is equivocal. Iron could have consumed O_2 when Fe^{3+}-oxyhydroxides formed in the oceans, or promoted atmospheric oxidation via pyrite burial. Through high-precision Fe isotopic measurements of Archean-Paleoproterozoic sediments and laboratory grown pyrites, we show that the triple-Fe-isotopic composition of Neoarchean-Paleoproterozoic pyrites requires both extensive marine iron oxidation and sulfide-limited pyritization. Using an isotopic fractionation model informed by these data, we constrain the relative sizes of sedimentary Fe^{3+}-oxyhydroxide and pyrite sinks for Neoarchean marine iron. We show that pyrite burial could have resulted in O_2 export exceeding local Fe^{2+} oxidation sinks, thus contributing to early episodes of transient oxygenation of Archean surface environments.

Main Text

Irreversible changes to oxic and euxinic sedimentary iron sinks during the Archean and Paleoproterozoic were intimately linked with the oxygenation of Earth's atmosphere during the Great Oxygenation Event (GOE) beginning *ca*. 2.43 Ga (*1*, *2*). Early oxygenation coincided with enhanced sedimentary burial of iron sulfide (pyrite) driven by the greater availability of sulfate (*3*–*5*). Through the pyrite iron sink, enhanced volcanic SO_2 fluxes in the Neoarchean could have indirectly induced the release of oxygen via the microbial reduction of volcanically-derived sulfate and the sequestration of sulfide in sedimentary pyrite (*6*–*8*). Meanwhile, iron could have acted as a net sink of oxygen produced during oxygenic photosynthesis, if Fe^{2+} dissolved in the oceans was not sequestered in sediments as pyrite, but rather as Fe^{3+}-oxyhydroxides. It is presently unknown if the balance of iron oxyhydroxide and pyrite sinks in certain marine sediments resulted in the net production or removal of oxygen in the period leading to the GOE.

Sedimentary Fe isotopic records show large shifts across the GOE (*9*, *10*) (Fig. 1A), and reflect evolution of the Fe, S, and O cycles through the Archean and Paleoproterozoic (*11*). Pre-GOE pyrites can have $^{56}Fe/^{54}Fe$ ratios shifted by up to -3.5‰ relative to most terrestrial rocks, a degree of fractionation rarely seen in the post-GOE rock record (*9*). The interpretation of these pyrite Fe isotopic compositions is not straightforward, because they could be controlled by (*i*) the size of oxidizing iron sinks that removed isotopically heavy Fe^{3+}-oxyhydroxides, leaving an isotopically light dissolved Fe^{2+} pool from which pyrite formed (*9*, *10*); (*ii*) microbial dissimilatory Fe^{3+} reduction (DIR) that preferentially releases an isotopically light Fe^{2+} pool (*12*, *13*); and (*iii*) a kinetic isotope effect (KIE) accompanying partial pyrite precipitation, which produces isotopically light pyrite (*14*, *15*). The relative importance of these processes remains debated (*9*–*18*), and this uncertainty has hindered quantitative interpretation of the ancient iron cycle, exemplified by the fact that Fe isotope records have not yet constrained the degree to which Fe removal on highly productive continental margins was a net sink or source for early O_2 (*8*).

Here, we report triple-Fe-isotopic ratio measurements that allow us to remove ambiguities in interpretations of the pre-GOE iron cycle. This approach relies on our discovery that the main isotopic fractionation processes implicated in the formation of pre-GOE pyrites follow distinct isotopic mass fractionation laws (MFLs), which describe how different isotopic ratios of the same element covary (*19*, *20*). To resolve MFLs, measurement of Fe isotopic ratios must be at higher precision than is typically reported in analysis of ancient sediments. This approach has been used

in igneous geochemistry to show that Fe isotopic variations in magmatic olivine followed a kinetic MFL for diffusive transport (*21*), and in aqueous UV photo-oxidation experiments to investigate pathways to the deposition of iron formations (IF) (*22*). Measurements of this type, to a comparable or higher precision, are used more frequently in cosmochemistry to resolve nucleosynthetic anomalies in meteorite samples (*23–26*). For a given MFL, the ratio of $^{56}Fe/^{54}Fe$ to that of $^{57}Fe/^{54}Fe$ defines the slope

$$\theta^{56/57} = \Delta\delta'^{56}Fe/\Delta\delta'^{57}Fe, \quad \text{(Eq. 1)}$$

where $\Delta\delta'^{x}Fe$ is a change in $\delta'^{x}Fe$; where $\delta'^{x}Fe$ (‰) = 1000 $\ln[(^{x}Fe/^{54}Fe)_{sample}/(^{x}Fe/^{54}Fe)_{IRMM\text{-}014}]$; imparted by physical, chemical, or biological processes. The $\Delta\delta'^{x}Fe$ for natural samples is taken as the difference from the bulk silicate Earth, which is approximated by IRMM-014 (*20*, *22*, *23*, *26*). As discussed below, we also ran pyrite synthesis experiments and there the $\Delta\delta'^{x}Fe$ value is taken as the difference from the starting material for each experiment. Isotopic trends following an array of MFLs are by definition mass-dependent. Apparent departures ($\epsilon'^{56}Fe$) from an arbitrary reference MFL (*20*, *23*, *27*), which we choose here to be the high-temperature equilibrium limit law with $\theta^{56/57}$=(1/53.939-1/55.935)/(1/53.939-1/56.935)=0.678, are defined as,

$$\epsilon'^{56}Fe = (\Delta\delta'^{56}Fe - 0.678 \times \Delta\delta'^{57}Fe) \times 10. \quad \text{(Eq. 2)}$$

In $\epsilon'^{56}Fe$ *vs.* $\Delta\delta'^{57}Fe$ space, MFLs form straight lines whose slopes can be related to $\theta^{56/57}$ through,

$$\epsilon'^{56}Fe = 10 \times (\theta^{56/57} - 0.678) \times \Delta\delta'^{57}Fe. \quad \text{(Eq. 3)}$$

In order to establish the values of $\theta^{56/57}$ corresponding to two end-member hypotheses that have been put forward to explain the $\delta'^{56}Fe$ pyrite record (*9*, *10*, *14*), we measured:

(*i*) A suite of IF samples that show a large range in $\delta'^{56}Fe$ values, including low $\delta'^{56}Fe$ values that most likely reflect precipitation from an iron pool that had experienced extensive iron oxidation (*28*) (Table S1). These samples are well-suited to characterize the MFL expected if sedimentary pyrite formed from a distilled pool of Fe^{2+} enriched in light Fe isotopes (low $\delta'^{56}Fe$) by precipitation of heavy (high $\delta'^{56}Fe$) Fe^{3+}-oxyhydroxides.

(*ii*) Experimental products of pyrite synthesis via the FeS-H_2S pathway (Fig. S2, Table S2), which produced pyrite that is isotopically lighter by as much as -2.4‰ in $\delta'^{56}Fe$ relative to the initial FeS pool (Fig. S2) (*27*). In these experiments, we precipitated pyrite in anoxic conditions from an FeS precursor (*27*) following previously established protocols (*14*, *27*, *29*). The experiment yielded a pyrite precipitate and a residual FeS phase that were separated using a

calibrated sequential extraction (*14*), enabling us to measure the isotopic fractionation between the reactant and product (Fig. S2). This fractionation represents a unidirectional KIE associated with pyrite precipitation, because once formed pyrite is highly insoluble and does not readily exchange with iron in solution. These pyrite samples represent a cumulative product reservoir rather than an instantaneous precipitate, but any deviations from an intrinsic Fe isotope MFL caused by cumulative effects are unresolvable within analytical uncertainties (*27*). Therefore, these experimental run products are well suited to characterize the MFL expected if sedimentary pyrite formation imparted a KIE on Fe isotopes.

The IFs, which were formed in the oceans after varying degrees of partial Fe^{2+} oxidation, define a slope of $\theta^{56/57}_{ox}$=0.6779±0.0006 for the oxidizing iron sink (here and elsewhere, the error bars are 95% confidence intervals), which agrees with iron photo-oxidation experiments (*22*) and is consistent with the view that equilibrium isotope exchange dominates during Fe^{2+} oxidation (*20*, *22*). The pyrite-precipitation experiments involving a KIE gave $\theta^{56/57}_{KIE}$=0.6743±0.0005. Triple-Fe-isotopic slopes for the two end-member scenarios are measurably distinct (Fig. 1B). Thus, we can use these slopes to address what caused Fe isotopic variations in pre-GOE sedimentary pyrites.

We analyzed a suite of pre-GOE Neoarchean-Paleoproterozoic (2.66-2.32 Ga) pyrites with depleted δ'^{56}Fe values (as low as -3.1‰) and four black shales from the same formations (Fig. 1A, Table S1). The pyrites and shales fall in an intermediate space on the triple-Fe-isotopic diagram between the endmember MFLs for Fe oxidation and pyrite precipitation (Fig. 1B). We do not interpret this data array as following a single MFL, because the pyrite and shale samples come from several distinct formations and each sample requires contributions from more than one fractionation process (with distinct MFLs). More likely, pre-GOE pyrite and shale δ'^{56}Fe values record a two-step process; partial marine Fe^{2+} oxidation during upwelling of Fe^{2+}-rich deep waters (*9*), and subsequent kinetic fractionation during partial, sulfide-limited pyrite formation from the remaining Fe^{2+} reservoir (*14*, *15*, *30*). In this model, Fe-oxyhydroxide and pyrite sinks sequestered iron upwelling from deep oceans lacking a discrete redoxcline that allowed progressive partial Fe^{2+} oxidation, towards black shale depositional settings (Figs. 2A, S7) (*10*, *27*, *31*). The loss of such depleted $\delta'^{56}Fe_{py}$ values after the GOE, which incidentally would prevent us resolving of MFLs for younger samples, indicates that prevailing conditions of sulfide-limitation, and progressive

136 partial Fe oxidation, were diminished following biogeochemical overturn taking place from 2.32
137 Ga (*11*).

138 The pyrite samples that we analyzed are nodular, deforming sedimentary laminations around
139 them, and must have formed in the sediment during early diagenesis. They most likely inherited
140 their Fe isotopic compositions from pyrite precipitated in porewater near the sediment-seawater
141 interface, but in some cases dissolution-reprecipitation has eradicated their primary textural
142 features and caused recrystallization into massive forms. *In situ* work on Archean pyrites suggests
143 that these secondary texture-altering processes do not eradicate primary sedimentary Fe isotopic
144 signatures (*18*). A major source of iron to porewaters would have been downward diffusion of
145 overlying Fe^{2+}-rich seawater into the sediments (*9*). The crux of the debate is whether pyrite simply
146 inherited the Fe isotopic composition of seawater, which was by far the largest exchangeable Fe
147 reservoir, or whether some kinetic isotopic fractionation was expressed, if pyritization was
148 incomplete due to limited sulfide supply. The new triple-Fe-isotopic measurements reported here
149 indicate that the latter case was true for the low $\delta'^{56}Fe$ pre-GOE pyrites we studied.

150 For any isotopically light pyrite sample, we can estimate contributions to the $\delta'^{56}Fe$ value from
151 prior oxidation of the Fe^{2+} pool, and the KIE during pyritization. To do so, we first calculate
152 contributions of Fe-oxidation to $\delta'^{56}Fe$ values of the water mass ($\delta'^{56}Fe_w$) from which pyrite
153 formed, from intercepts of the kinetic pyritization MFL passing through individual datapoints with
154 the oxidation MFL (Fig. 2B). We then determine the Fe isotopic fractionation imparted by
155 pyritization by taking the difference in $\delta'^{56}Fe$ values between those of pyrite and $\delta'^{56}Fe_w$ (Figs. 2B,
156 S5) (*27*).

157 Our approach assumes that partial iron oxidation and pyritization were the main drivers of
158 $\delta'^{56}Fe$ variations in sedimentary pyrite. It is however conceivable that some porewater or marine
159 Fe^{2+} was sourced from DIR (*12*, *13*, *32*), a microbial metabolism that seems to have been active
160 since at least 3.2 Ga (*18*). This represents a source of uncertainty in our model. Experiments to
161 date suggest that the isotopic fractionation during DIR reflects equilibration of Fe^{2+} and Fe^{3+} after
162 the reduction step (*33*), and therefore we expect that it would fall into the same class of redox
163 equilibrium processes that define the Fe^{2+} oxidation MFL. The observed departure of natural pyrite
164 from this MFL therefore implies that regardless of the potential role of DIR, a KIE during
165 pyritization is also required to explain pre-GOE $\delta'^{56}Fe_{py}$ values.

The fraction of Fe^{3+}-oxyhydroxide removed to give the $\delta'^{56}Fe_w$ value on the intercept (F_{ox}=Fe in oxyhydroxide sink/total Fe sink), and the fraction of pyrite removed from that remaining Fe^{2+} pool (f_{py}=Fe in pyrite/Fe remaining after Fe removal to the oxyhydroxide sink), were calculated under Rayleigh fractionation conditions (Figs. 2, S5; Table S5). The setting that we envision is progressive Fe^{2+} oxidation as Fe^{2+}-rich deep-waters are upwelled towards more oxidizing photic zone conditions (*9*, *10*) (Fig., S7). We also explored a 1-D dispersion-reaction steady-state model for water-column Fe^{2+} oxidation, and find that our conclusions using Rayleigh distillation are robust (*27*, *34*). We treated pyrite as a cumulative product of pyritization (*27*). The fractional pyrite sink, F_{py}, for iron in the whole depositional system is $F_{py}=f_{py} \times (1-F_{ox})$. In Fig. 2D, we plot contours of constant F_{ox}/F_{py}, showing that $\epsilon'^{56}Fe$ measurements are diagnostic of the relative size of the oxide and pyrite iron sinks.

To fully propagate the effect of uncertainties in sample measurements and $\theta^{56/57}$ values for the end-member processes on uncertainties in F_{ox}, f_{py}, and F_{py}, we used a Monte-Carlo simulation (Fig. 3). Estimates for F_{py} span 10 to 80 % of the upwelled iron pool (within 95 % confidence interval) for the low $\delta'^{56}Fe$ pyrites that we studied. With initial pre-GOE deep-water [Fe^{2+}] concentration ~50 μM (*1*), the pyrite sink could have removed 5 to 40 μM of dissolved iron. This requires ~10 to 80 μM of seawater-dissolved sulfate to be microbially reduced to sulfide, ~350 to 1,400 times less than the modern seawater sulfate concentration of 28 mM, but within recent estimates for Archean seawater sulfate based on S isotope modelling (*35*, *36*). For the ~2.65 Ga Jeerinah and Lokammona formations, we infer that as little as 10% of iron upwelled onto the shelf was deposited as pyrite (Figs. 2C, 3, S6) (*27*).

When volcanic SO_2 is the primary sulfur source, burial of reduced sulfur in pyrite represents a net oxidation of Earth's surface (*6*–*8*) (Fig. 2A). For example, the reaction $2SO_2 + H_2O + Fe^{2+} \rightarrow FeS_2 + 2H^+ + 2.5O_2$; describing the net effect of SO_2 photolysis and hydrolysis, cyanobacterial photosynthesis, microbial sulfate reduction, and pyrite precipitation; indicates that pyrite burial can indirectly drive net O_2 export to the atmosphere-ocean system (*8*). The reaction provides a maximum estimate for O_2 export during pyrite burial because: (*i*) a more reduced original sulfur source would weaken the net oxidative effect of pyrite burial, and (*ii*) other types of primary productivity, such as anoxygenic photoferrotrophy, which oxidizes Fe^{2+} directly, could have contributed organic matter for sulfate reduction, but only cyanobacterial activity would have

196 produced O_2. A more realistic estimate for the volcanic H_2S/SO_2 emission ratio at ~1 (*7*) would
197 result in a net 1 mole O_2 yield per mole of pyrite buried.
198 To oxygenate the atmosphere via pyrite burial, the produced O_2 would also need to overcome
199 O_2 buffers in the ocean, primarily the upwelled Fe^{2+} flux (Fig. 2A). Oxygen-driven Fe^{2+} oxidation
200 consumes 0.25 moles of O_2 per mole of Fe^{3+} buried, so net O_2 sources and sinks will be balanced
201 when F_{ox}/F_{py} is 4 and 10 for volcanic H_2S/SO_2 emission ratios of 1 (*7*) and 0 (*8*), respectively.
202 Depending on F_{ox}/F_{py} ratios, iron deposition on productive continental margins could have been a
203 net source or sink for O_2 in the atmosphere-ocean system. Triple-Fe-isotopic systematics are
204 diagnostic of F_{ox}/F_{py} ratios (Fig. 2D). Pre-GOE pyrite data all fall above the F_{ox}/F_{py}=4 contour, and
205 the F_{ox}/F_{py}=10 contour is outside of the error bar on pyrite ϵ'^{56}Fe values. We can therefore rule out
206 net O_2 sink-like behavior for the case where SO_2 dominated Neoarchean volcanic emissions. Even
207 with a conservative volcanic H_2S/SO_2 ratio of 1 (*7*), our data support a net O_2 source in Neoarchean
208 pyrite-forming environments, particularly after 2.52 Ga (Figs. 2D, 3). The inference that the oxic
209 sink did not overwhelm local oxygen sources associated with pyrite deposition also holds if F_{ox} is
210 calculated using a 1-D dispersion-reaction model (*27*, *34*). Average results from Monte Carlo
211 simulations imply that even in the cases where we find the smallest F_{py} and largest F_{ox}, in ~2.65
212 Ga Jeerinah and Lokamonna formation pyrites, some O_2 could have been exported to the
213 atmosphere-ocean system during pyrite burial after exhausting local Fe^{2+} oxidation sinks. We
214 focused on the lowest δ'^{56}Fe pyrites because these give us the most leverage to characterize MFLs.
215 Pre-GOE pyrites, while displaying much more negative δ'^{56}Fe values (average of about -2 ‰) than
216 post-GOE pyrites (Fig. 1A), span a range of values. The more typical pyrites could have formed
217 from a seawater reservoir that did not experience such protracted Fe^{2+} oxidation (*9*, *10*) or may
218 reflect higher degrees of pyritization. The amount of oxygen produced in such settings (moles of
219 O_2 generated per mole of pyrite buried) would have been higher than the values calculated here
220 for the isotopically lightest pyrites. The conclusion that iron oxide burial did not locally buffer O_2
221 generated by pyrite burial in the Neoarchean is therefore robust.
222 The triple-Fe-isotopic proxy provides new insights into the iron cycle in Earth's early oceans.
223 Before the GOE, large and probably fluctuating hydrothermal and riverine iron fluxes to the oceans
224 (*31*) were removed to two sedimentary sinks (Figs. 2A, S7) (*27*). The major sink was
225 Fe^{3+}-oxyhydroxides that were deposited from upwelling water masses in the oceans that lacked a
226 discrete redoxcline and allowed protracted partial iron oxidation (*9*, *10*). The second iron sink was

227 on highly productive continental margins, where deposition of pyrite-rich sediments was generally
228 sulfide-limited due to a small marine sulfate pool. Small relative changes in iron removal to these
229 oxyhydroxide and sulfide sinks potentially led to perturbations in the net O_2 supply to the
230 atmosphere-ocean system that fueled shallow-marine oxygen oases (*37*, *38*) and helped prime the
231 Earth system for 'whiffs' of atmospheric O_2 in the runup to the GOE (*39*).
232

References and Notes

1. H. D. Holland, *The Chemical Evolution of the Atmosphere and Oceans* (Princeton University Press, 1984).

2. A. P. Gumsley, K. R. Chamberlain, W. Bleeker, U. Söderlund, M. O. de Kock, E. R. Larsson, A. Bekker, Timing and tempo of the Great Oxidation Event. *Proc. Natl. Acad. Sci.* **114**, 1811–1816 (2017).

3. C. T. Scott, A. Bekker, C. T. Reinhard, B. Schnetger, B. Krapež, D. Rumble, T. W. Lyons, Late Archean euxinic conditions before the rise of atmospheric oxygen. *Geology*. **39**, 119–122 (2011).

4. C. T. Reinhard, R. Raiswell, C. Scott, A. D. Anbar, T. W. Lyons, A Late Archean Sulfidic Sea Stimulated by Early Oxidative Weathering of the Continents. *Science*. **326**, 713–716 (2009).

5. E. E. Stüeken, D. C. Catling, R. Buick, Contributions to late Archaean sulphur cycling by life on land. *Nat. Geosci.* **5**, 722–725 (2012).

6. L. R. Kump, M. E. Barley, Increased subaerial volcanism and the rise of atmospheric oxygen 2.5 billion years ago. *Nature*. **448**, 1033–1036 (2007).

7. F. Gaillard, B. Scaillet, N. T. Arndt, Atmospheric oxygenation caused by a change in volcanic degassing pressure. *Nature*. **478**, 229–232 (2011).

8. S. L. Olson, C. M. Ostrander, D. D. Gregory, M. Roy, A. D. Anbar, T. W. Lyons, Volcanically modulated pyrite burial and ocean–atmosphere oxidation. *Earth Planet. Sci. Lett.* **506**, 417–427 (2019).

9. O. J. Rouxel, A. Bekker, K. J. Edwards, Iron Isotope Constraints on the Archean and Paleoproterozoic Ocean Redox State. *Science*. **307**, 1088–1091 (2005).

10. N. Planavsky, O. J. Rouxel, A. Bekker, A. Hofmann, C. T. S. Little, T. W. Lyons, Iron isotope composition of some Archean and Proterozoic iron formations. *Geochim. Cosmochim. Acta*. **80**, 158–169 (2012).

11. A. W. Heard, N. Dauphas, Constraints on the coevolution of oxic and sulfidic ocean iron sinks from Archean–Paleoproterozoic iron isotope records. *Geology*. **48**, 358–362 (2020).

12. B. L. Beard, C. M. Johnson, L. Cox, H. Sun, K. H. Nealson, C. Aguilar, Iron Isotope Biosignatures. *Science*. **285**, 1889–1892 (1999).

13. C. Archer, D. Vance, Coupled Fe and S isotope evidence for Archean microbial Fe(III) and sulfate reduction. *Geology*. **34**, 153–156 (2006).

14. R. Guilbaud, I. B. Butler, R. M. Ellam, Abiotic Pyrite Formation Produces a Large Fe Isotope Fractionation. *Science*. **332**, 1548–1551 (2011).

15. J. M. Rolison, C. H. Stirling, R. Middag, M. Gault-Ringold, E. George, M. J. A. Rijkenberg, Iron isotope fractionation during pyrite formation in a sulfidic Precambrian ocean analogue. *Earth Planet. Sci. Lett.* **488**, 1–13 (2018).

16. N. Dauphas, S. G. John, O. Rouxel, Iron Isotope Systematics. *Rev. Mineral. Geochem.* **82**, 415–510 (2017).

17. J. Marin-Carbonne, C. Rollion-Bard, A. Bekker, O. Rouxel, A. Agangi, B. Cavalazzi, C. C. Wohlgemuth-Ueberwasser, A. Hofmann, K. D. McKeegan, Coupled Fe and S isotope variations in pyrite nodules from Archean shale. *Earth Planet. Sci. Lett.* **392**, 67–79 (2014).

18. J. Marin-Carbonne, V. Busigny, J. Miot, C. Rollion-Bard, E. Muller, N. Drabon, D. Jacob, S. Pont, M. Robyr, T. R. R. Bontognali, C. François, S. Reynaud, M. V. Zuilen, P. Philippot, In Situ Fe and S isotope analyses in pyrite from the 3.2 Ga Mendon Formation (Barberton Greenstone Belt, South Africa): Evidence for early microbial iron reduction. *Geobiology*. **n/a** (2020), doi:10.1111/gbi.12385.

19. E. D. Young, A. Galy, H. Nagahara, Kinetic and equilibrium mass-dependent isotope fractionation laws in nature and their geochemical and cosmochemical significance. *Geochim. Cosmochim. Acta*. **66**, 1095–1104 (2002).

20. N. Dauphas, E. A. Schauble, Mass Fractionation Laws, Mass-Independent Effects, and Isotopic Anomalies. *Annu. Rev. Earth Planet. Sci.* **44**, 709–783 (2016).

21. A. J. McCoy-West, J. G. Fitton, M.-L. Pons, E. C. Inglis, H. M. Williams, The Fe and Zn isotope composition of deep mantle source regions: Insights from Baffin Island picrites. *Geochim. Cosmochim. Acta*. **238**, 542–562 (2018).

22. N. X. Nie, N. Dauphas, R. C. Greenwood, Iron and oxygen isotope fractionation during iron UV photo-oxidation: Implications for early Earth and Mars. *Earth Planet. Sci. Lett.* **458**, 179–191 (2017).

23. N. Dauphas, D. L. Cook, A. Sacarabany, C. Fröhlich, A. M. Davis, M. Wadhwa, A. Pourmand, T. Rauscher, R. Gallino, Iron 60 Evidence for Early Injection and Efficient Mixing of Stellar Debris in the Protosolar Nebula. *Astrophys. J.* **686**, 560–569 (2008).

24. M. Schiller, M. Bizzarro, J. Siebert, Iron isotope evidence for very rapid accretion and differentiation of the proto-Earth. *Sci. Adv.* **6**, eaay7604 (2020).

25. H. Tang, N. Dauphas, Abundance, distribution, and origin of 60Fe in the solar protoplanetary disk. *Earth Planet. Sci. Lett.* **359–360**, 248–263 (2012).

26. H. Tang, N. Dauphas, P. R. Craddock, High Precision Iron Isotopic Analyzes Of Meteorites And Terrestrial Rocks: ^{60}Fe Distribution And Mass Fractionation Laws. *LPS XXXX*. **40**, 1903 (2009).

27. Materials and methods are available as supplementary materials on Science Online.

28. H. Tsikos, A. Matthews, Y. Erel, J. M. Moore, Iron isotopes constrain biogeochemical redox cycling of iron and manganese in a Palaeoproterozoic stratified basin. *Earth Planet. Sci. Lett.* **298**, 125–134 (2010).

29. D. Rickard, Kinetics of pyrite formation by the H2S oxidation of iron (II) monosulfide in aqueous solutions between 25 and 125°C: The rate equation. *Geochim. Cosmochim. Acta.* **61**, 115–134 (1997).

30. O. J. Rouxel, A. Bekker, K. J. Edwards, Response to Comment on "Iron Isotope Constraints on the Archean and Paleoproterozoic Ocean Redox State." *Science*. **311**, 177–177 (2006).

31. A. Bekker, J. F. Slack, N. Planavsky, B. Krapež, A. Hofmann, K. O. Konhauser, O. J. Rouxel, Iron Formation: The Sedimentary Product of a Complex Interplay among Mantle, Tectonic, Oceanic, and Biospheric Processes. *Econ. Geol.* **105**, 467–508 (2010).

32. S. Severmann, T. W. Lyons, A. Anbar, J. McManus, G. Gordon, Modern iron isotope perspective on the benthic iron shuttle and the redox evolution of ancient oceans. *Geology*. **36**, 487–490 (2008).

33. Crosby Heidi A., Roden Eric E., Johnson Clark M., Beard Brian L., The mechanisms of iron isotope fractionation produced during dissimilatory Fe(III) reduction by Shewanella putrefaciens and Geobacter sulfurreducens. *Geobiology*. **5**, 169–189 (2007).

34. A. D. Czaja, C. M. Johnson, E. E. Roden, B. L. Beard, A. R. Voegelin, T. F. Nägler, N. J. Beukes, M. Wille, Evidence for free oxygen in the Neoarchean ocean based on coupled iron–molybdenum isotope fractionation. *Geochim. Cosmochim. Acta*. **86**, 118–137 (2012).

35. J. W. Jamieson, B. A. Wing, J. Farquhar, M. D. Hannington, Neoarchaean seawater sulphate concentrations from sulphur isotopes in massive sulphide ore. *Nat. Geosci.* **6**, 61–64 (2013).

36. S. A. Crowe, G. Paris, S. Katsev, C. Jones, S.-T. Kim, A. L. Zerkle, S. Nomosatryo, D. A. Fowle, J. F. Adkins, A. L. Sessions, J. Farquhar, D. E. Canfield, Sulfate was a trace constituent of Archean seawater. *Science*. **346**, 735–739 (2014).

37. S. L. Olson, L. R. Kump, J. F. Kasting, Quantifying the areal extent and dissolved oxygen concentrations of Archean oxygen oases. *Chem. Geol.* **362**, 35–43 (2013).

38. C. M. Ostrander, S. G. Nielsen, J. D. Owens, B. Kendall, G. W. Gordon, S. J. Romaniello, A. D. Anbar, Fully oxygenated water columns over continental shelves before the Great Oxidation Event. *Nat. Geosci.* **12**, 186–191 (2019).

39. A. D. Anbar, Y. Duan, T. W. Lyons, G. L. Arnold, B. Kendall, R. A. Creaser, A. J. Kaufman, G. W. Gordon, C. Scott, J. Garvin, R. Buick, A Whiff of Oxygen Before the Great Oxidation Event? *Science*. **317**, 1903–1906 (2007).

40. D. Rickard, G. W. Luther, Chemistry of Iron Sulfides. *Chem. Rev.* **107**, 514–562 (2007).

41. D. Rickard, A. Griffith, A. Oldroyd, I. B. Butler, E. Lopez-Capel, D. A. C. Manning, D. C. Apperley, The composition of nanoparticulate mackinawite, tetragonal iron(II) monosulfide. *Chem. Geol.* **235**, 286–298 (2006).

42. N. Dauphas, A. Pourmand, F.-Z. Teng, Routine isotopic analysis of iron by HR-MC-ICPMS: How precise and how accurate? *Chem. Geol.* **267**, 175–184 (2009).

43. P. R. Craddock, N. Dauphas, Iron Isotopic Compositions of Geological Reference Materials and Chondrites. *Geostand. Geoanalytical Res.* **35**, 101–123 (2011).

44. J. Farquhar, D. T. Johnston, B. A. Wing, K. S. Habicht, D. E. Canfield, S. Airieau, M. H. Thiemens, Multiple sulphur isotopic interpretations of biosynthetic pathways: implications for biological signatures in the sulphur isotope record. *Geobiology*. **1**, 27–36 (2003).

45. I. N. Bindeman, D. O. Zakharov, J. Palandri, N. D. Greber, N. Dauphas, G. J. Retallack, A. Hofmann, J. S. Lackey, A. Bekker, Rapid emergence of subaerial landmasses and onset of a modern hydrologic cycle 2.5 billion years ago. *Nature*. **557**, 545 (2018).

46. B. L. Beard, C. M. Johnson, K. L. V. Damm, R. L. Poulson, Iron isotope constraints on Fe cycling and mass balance in oxygenated Earth oceans. *Geology*. **31**, 629–632 (2003).

47. M. Mansor, M. S. Fantle, A novel framework for interpreting pyrite-based Fe isotope records of the past. *Geochim. Cosmochim. Acta*. **253**, 39–62 (2019).

48. V. B. Polyakov, R. N. Clayton, J. Horita, S. D. Mineev, Equilibrium iron isotope fractionation factors of minerals: Reevaluation from the data of nuclear inelastic resonant X-ray scattering and Mössbauer spectroscopy. *Geochim. Cosmochim. Acta*. **71**, 3833–3846 (2007).

49. A. F. Trendall, R. C. Morris, *Iron-Formation: Facts and Problems* (Elsevier, 2000).

50. K. O. Konhauser, T. Hamade, R. Raiswell, R. C. Morris, F. G. Ferris, G. Southam, D. E. Canfield, Could bacteria have formed the Precambrian banded iron formations? *Geology*. **30**, 1079–1082 (2002).

51. A. Kappler, C. Pasquero, K. O. Konhauser, D. K. Newman, Deposition of banded iron formations by anoxygenic phototrophic Fe(II)-oxidizing bacteria. *Geology*. **33**, 865–868 (2005).

52. C. Klein, Some Precambrian banded iron-formations (BIFs) from around the world: Their age, geologic setting, mineralogy, metamorphism, geochemistry, and origins. *Am. Mineral.* **90**, 1473–1499 (2005).

53. F. J. Millero, S. Sotolongo, M. Izaguirre, The oxidation kinetics of Fe(II) in seawater. *Geochim. Cosmochim. Acta*. **51**, 793–801 (1987).

54. S. Moorbath, R. K. O'nions, R. J. Pankhurst, Early Archaean Age for the Isua Iron Formation, West Greenland. *Nature*. **245**, 138 (1973).

55. F. Thibon, J. Blichert-Toft, H. Tsikos, J. Foden, E. Albalat, F. Albarede, Dynamics of oceanic iron prior to the Great Oxygenation Event. *Earth Planet. Sci. Lett.* **506**, 360–370 (2019).

56. N. Dauphas, M. van Zuilen, M. Wadhwa, A. M. Davis, B. Marty, P. E. Janney, Clues from Fe Isotope Variations on the Origin of Early Archean BIFs from Greenland. *Science*. **306**, 2077–2080 (2004).

57. A. Angert, S. Rachmilevitch, E. Barkan, B. Luz, Effects of photorespiration, the cytochrome pathway, and the alternative pathway on the triple isotopic composition of atmospheric O2. *Glob. Biogeochem. Cycles*. **17**, 1030 (2003).

58. X. Cao, Y. Liu, Equilibrium mass-dependent fractionation relationships for triple oxygen isotopes. *Geochim. Cosmochim. Acta*. **75**, 7435–7445 (2011).

59. E. D. Young, L. Y. Yeung, I. E. Kohl, On the Δ17O budget of atmospheric O2. *Geochim. Cosmochim. Acta*. **135**, 102–125 (2014).

60. N. E. Levin, T. D. Raub, N. Dauphas, J. M. Eiler, Triple oxygen isotope variations in sedimentary rocks. *Geochim. Cosmochim. Acta*. **139**, 173–189 (2014).

61. A. M. Davis, F. M. Richter, R. A. Mendybaev, P. E. Janney, M. Wadhwa, K. D. McKeegan, Isotopic mass fractionation laws for magnesium and their effects on 26Al–26Mg systematics in solar system materials. *Geochim. Cosmochim. Acta*. **158**, 245–261 (2015).

62. S. Ono, B. Wing, D. Johnston, J. Farquhar, D. Rumble, Mass-dependent fractionation of quadruple stable sulfur isotope system as a new tracer of sulfur biogeochemical cycles. *Geochim. Cosmochim. Acta*. **70**, 2238–2252 (2006).

63. D. T. Johnston, J. Farquhar, K. S. Habicht, D. E. Canfield, Sulphur isotopes and the search for life: strategies for identifying sulphur metabolisms in the rock record and beyond. *Geobiology*. **6**, 425–435 (2008).

64. J. Zhang, S. Huang, A. M. Davis, N. Dauphas, A. Hashimoto, S. B. Jacobsen, Calcium and titanium isotopic fractionations during evaporation. *Geochim. Cosmochim. Acta*. **140**, 365–380 (2014).

65. K. O. Konhauser, N. J. Planavsky, D. S. Hardisty, L. J. Robbins, T. J. Warchola, R. Haugaard, S. V. Lalonde, C. A. Partin, P. B. H. Oonk, H. Tsikos, T. W. Lyons, A. Bekker, C. M. Johnson, Iron formations: A global record of Neoarchaean to Palaeoproterozoic environmental history. *Earth-Sci. Rev*. **172**, 140–177 (2017).

66. S. A. Welch, B. L. Beard, C. M. Johnson, P. S. Braterman, Kinetic and equilibrium Fe isotope fractionation between aqueous Fe(II) and Fe(III). *Geochim. Cosmochim. Acta*. **67**, 4231–4250 (2003).

Acknowledgments: Discussions with Stephanie Olson Jake Waldbauer, Sarah Aarons, and Sam Holo were appreciated. Nigel Brauser and Anne Davis are thanked for comments on the clarity of the manuscript. We thank Angelo Olinto, James Passolano, Dan DeYoung, James Eason, Michael Grosse, Fred Ciesla, Kimberly Mormann, Jolene Hanchar, Sarah Lippert, Ronald Klain, Victor Gavin, Steven Bandyk, Alfredo Peralta, Chris Kielch, Thomas Indelli, Timo Hopp, and Mike Andrews and the UJAMAA Construction team for renovating our laboratory infrastructure and supporting its operation. This work was funded by NASA grants 80NSSC17K0744 to ND and AWH (Habitable Worlds), 359NNX17AE86G to ND (LARS), NNX17AE87G and 80NSSC20K0821 to ND (Emerging Worlds), and NSF grant EAR-2001098 to ND (CSEDI). AWH was supported by an Eckhardt Scholarship from the University of Chicago. Participation by AB was supported by NSERC Discovery and Acceleration grants.

Author contributions: AWH, ND, and NXN initiated the study. OJR and AB provided samples. AWH, RG, and IBB performed the pyrite synthesis experiments. AWH and NXN measured iron isotopic compositions. AWH and ND performed modeling. All authors contributed to interpretation of results. AWH, ND, and AB wrote the first draft of the manuscript, which was subsequently edited with input from all authors.

Competing financial interests: The authors declare that they have no competing financial interests.

Data availability: All original data are reported in Tables in the Supplementary Online Materials. Literature iron isotope data presented in Figure 1A are compiled in the EarthChem library at https://doi.org/10.1594/IEDA/111446.

List of Supplementary Materials:

Materials and Methods
Supplementary Text
Figs. S1 to S10
Tables S1 to S5
References 40-67

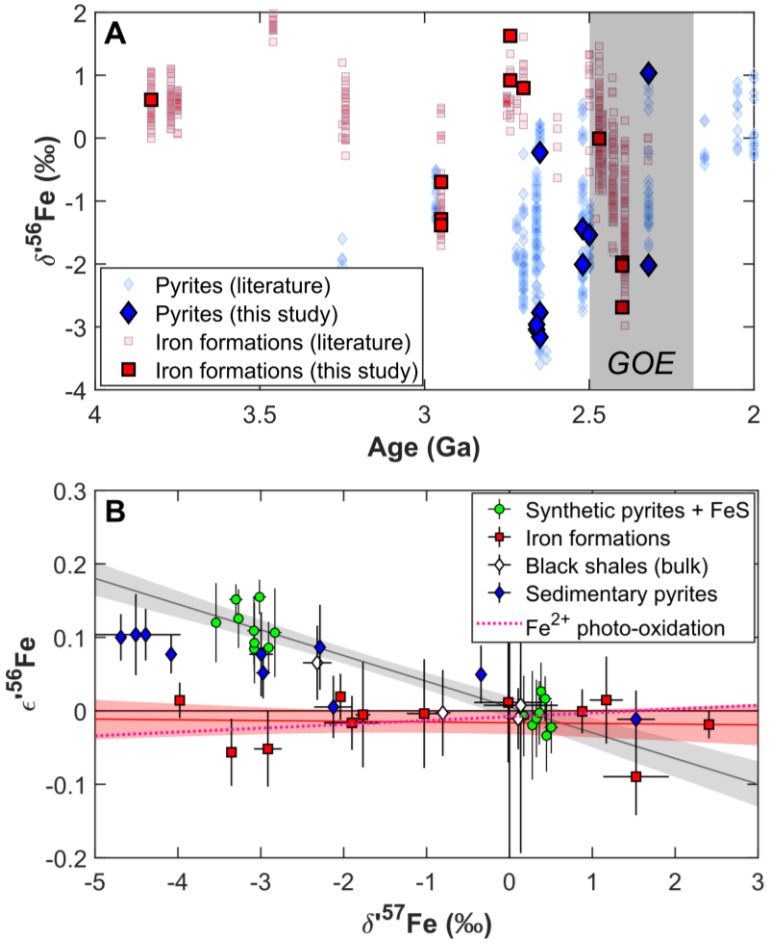

Fig. 1.

Iron isotope systematics of (*i*) pre-GOE sediments and natural pyrites, and (*ii*) synthetic pyrites and FeS produced in laboratory experiments (Tables S1, S2) (*27*). A. $\delta'^{56}Fe$ (relative to IRMM-014) values of IFs and pyrites analyzed in this study, plotted against their age (published IF and pyrite data compiled in (*11*) are also plotted for reference). B. Triple-Fe-isotopic systematics for IFs, pyrites, and black shales in $\epsilon'^{56}Fe$ *vs.* $\Delta\delta'^{57}Fe$ space. $\Delta\delta'^{57}Fe$ values are reported as differences from IRMM-014 and the starting material of experiments, for the natural samples and the synthetic pyrites, respectively. Error bars and envelopes are 95% confidence intervals. The slopes of end-member MFLs associated with iron-redox processes (red line and red envelope) and kinetic isotope effects (black line and grey envelope) during pyritization are constrained through analysis of isotopically light Mn-rich IFs and laboratory pyrite precipitated via the H_2S pathway (*14*, *27*, *40*), respectively. The slope of the IF MFL agrees well with the theoretical high-temperature equilibrium limit law (defined by the horizontal axis, (*20*)), and an experimentally determined

454 MFL for Fe^{2+} oxidation (via UV photo-oxidation (*22*)), implying control by Fe^{2+}-Fe^{3+} equilibrium.
455 Synthetic pyrite and FeS define a kinetic MFL for sulfide precipitation. Pre-GOE pyrites fall in an
456 intermediate space between redox-equilibrium and kinetic endmembers.

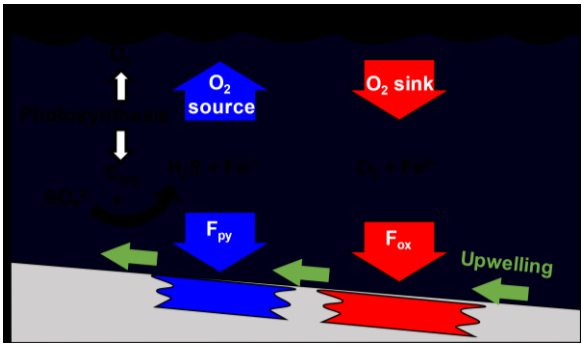
O2
Photosynthesis
O2 source
O2 sink
H2S + Fe2+
O2 + Fe2+
SO42-
Fpy
Fox
Upwelling

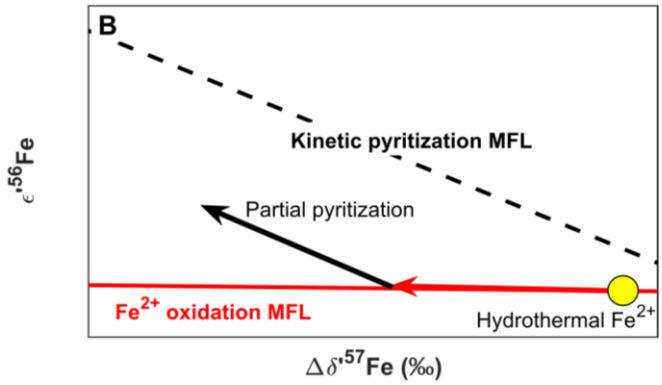
B
Kinetic pyritization MFL
Partial pyritization
Fe2+ oxidation MFL
Hydrothermal Fe2+
ε'56Fe
Δδ'57Fe (‰)

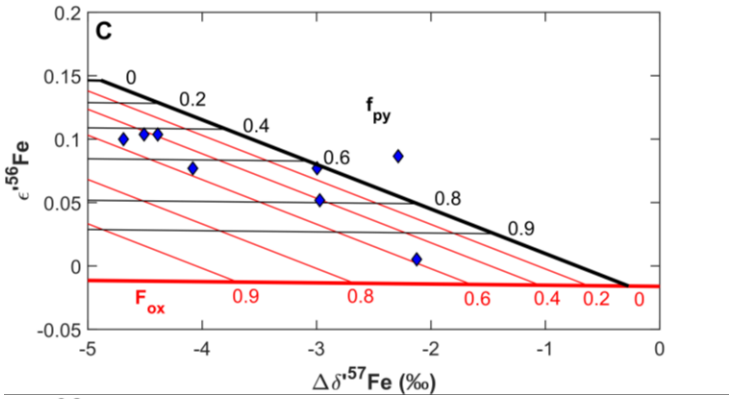
C
fpy
0
0.2
0.4
0.6
0.8
0.9
Fox
ε'56Fe
Δδ'57Fe (‰)

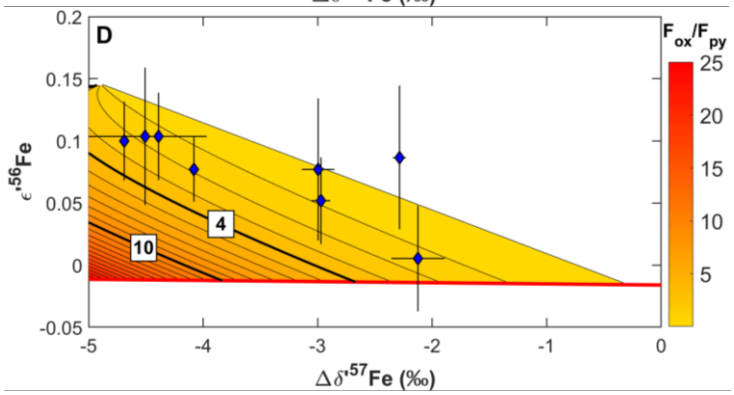
D
Fox/Fpy
4
10
ε'56Fe
Δδ'57Fe (‰)

Fig. 2.

Interpretation of triple-Fe-isotope compositions of isotopically light pyrites. A. Schematic representation of the Fe sinks (F_{ox} and F_{py}), and their inferred links to O_2 cycling in the pre-GOE oceans. B. Triple Fe isotopic interpretation of the two-step process involved in pyrite formation. Iron with starting composition resembling hydrothermal fluids (yellow circle; $\Delta\delta'^{57}Fe$=-0.3‰ relative to IRMM-014 with $\epsilon'^{56}Fe$ on the empirical MFL defined by IFs) is oxidized, driving residual Fe^{2+} to lighter $\delta'^{57}Fe$ compositions along the Fe^{2+} oxidation MFL. Partial pyrite precipitation from this residual Fe^{2+} subsequently causes fractionation along the kinetic pyritization MFL. The approach is detailed in Figure S5 with mathematical derivations provided in Supplementary Materials (*27*). C. Pyrite data and contours for F_{ox} and f_{py} in triple-Fe-isotopic space. Both Fe^{2+} oxidation and pyritization are modeled using Rayleigh distillations. Iron isotopic fractionation during iron oxidation is assumed to reflect the composition of residual dissolved Fe^{2+} experiencing fractional removal of Fe^{3+}-oxyhydroxide upon upwelling into oxidizing near surface waters. Iron isotopic fractionation during pyritization is assumed to reflect the composition of the cumulative product, as we analyzed relatively large pyrite nodules (*27*). The fraction of total upwelled Fe deposited as pyrite is calculated as $F_{py} = f_{py} \times (1 - F_{ox})$. D. Pyrite data and contours of F_{ox}/F_{py} (relative size of oxyhydroxide and pyrite sedimentary Fe sinks). Bold contours at 4 and 10 indicate thresholds for net O_2 source *vs*. sink behavior for volcanic H_2S/SO_2 inputs ratios of 1 (*7*) and 0 (*8*), respectively. In B.-D., $\Delta\delta'^{57}Fe$ values are reported as differences from IRMM-014.

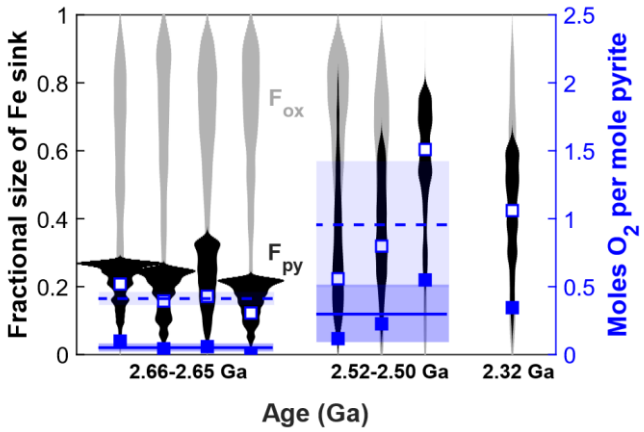

Fig. 3.

F_{ox} and F_{py}, and molar O_2 yield estimates from a Monte Carlo error propagation. Violin plots for probability densities of fractional size of Fe sink (grey: F_{ox}, black: F_{py}) determined from propagation of errors on the $\epsilon'^{56}Fe$ and $\Delta\delta'^{57}Fe$ values for each measured pyrite and the errors on the slopes of the MFLs (*27*). Blue filled and open squares: estimated molar O_2 yields per mole of pyrite buried for individual samples using H_2S/SO_2 input ratios of 1 (*7*) and 0 (*8*), respectively. Blue solid and dashed lines and shaded areas: mean molar O_2 yields for H_2S/SO_2 input ratios of 1 (*7*) and 0 (*8*), respectively, and 95% confidence intervals for pyrites in two age bins.

Science
AAAS

Supplementary Materials for

Resolving the Role of Ocean Iron Sinks in Early Atmospheric Oxygenation

Andy W. Heard, Nicolas Dauphas, Romain Guilbaud, Olivier J. Rouxel, Ian B. Butler, Nicole X. Nie, Andrey Bekker

Correspondence to: andyheard@uchicago.edu

This PDF file includes:

Materials and Methods

Methods

Pyrite synthesis experiments

To constrain the triple-Fe-isotopic expression of pyrite precipitation, we performed new laboratory pyrite precipitation experiments in an anoxic environment. Pyrite was synthesized at the University of Edinburgh, via the FeS-H_2S pathway following the methodology of Guilbaud et al. (2011) (*14*) and references therein, which produces pyrite precipitates from an FeS_m (mackinawite) reactant. We provide a brief overview here, and the detailed protocol is described below. First, we produced a solid FeS_m precursor by combining equimolar solutions of Fe^{2+} and sulfide. This solid reactant was filtered and freeze dried and then sealed into reaction vessels in a pH buffer solution. The sealed reaction vessels were then attached to a gas-mixing manifold and injected with a controlled volume of H_2S, which was generated by reacting sodium sulfide with sulfuric acid. The vessels were resealed, and the pyrite precipitation reaction was allowed to proceed for a few hours to a few days, after which pyrite and residual FeS were separated using a calibrated chemical extraction technique (*14*). We measured the triple-Fe-isotopic fractionation between FeS and pyrite, which has been shown previously to be the reaction where a large kinetic isotope effect is imparted to pyrite (*14*).

All reagents were of analytical grade, and solutions were prepared using 18 MΩ/cm deionized water and sparged for 30 min with O_2-free grade N_2 before use. Solutions were prepared and solid FeS_m was synthesized in N_2-filled recirculating Saffron alpha anoxic chamber under O_2-free conditions. FeS_m was precipitated by mixing 100 mL of 0.6 M iron (Fe^{2+}) solution prepared with Mohr's salt [$(NH_4)_2Fe(SO_4)_2 \cdot 6H_2O$; Sigma Aldrich] with 100 mL of 0.6 M sulfide solution made with $Na_2S \cdot 9H_2O$ (Sigma Aldrich). This reaction produced a black precipitate. The precipitate was filtered using a Buchner filter with Whatman™ No 1 filter paper, resuspended in sparged water and the filtration was repeated three times. The freshly precipitated FeS_m was freeze-dried overnight on a Mini-Lyotrap (LTE) freeze-dryer then transferred back to the anoxic chamber and stored under O_2-free conditions until use. The low-metal complexing MOPS (3-(N-morpholino)propanesulfonic acid, pKa = 7.31, Fisher) buffer was made by dissolution of its sodium salt in sparged water, buffered to pH 6 by NaOH titration. Redox buffer Ti^{3+} citrate, required for poising the Eh during sample recovery, was prepared by adding 5 mL 15% $TiCl_3$ to 50 mL 0.2 M Na citrate and buffered to pH 7 with Na_2CO_3. The solutions were stored in the glove box under O_2-free conditions until use.

The pyrite precipitation experiments were prepared in the glove box. Approximately 300 mg of the freeze-dried FeS_m was weighed into serum bottles, 10 mL of 0.05 M MOPS buffer solution was added, and the bottles were sealed with rubber stoppers and aluminum crimper seals. The sealed bottles were attached to a gas transfer manifold via a hypodermic needle inserted through the rubber stopper, and the manifold and reaction bottle were flushed with O_2-free grade N_2 and pumped down to -14 PSI (-97 kPa) three times. A sealed serum bottle containing 800 mg solid $Na_2S \cdot 9H_2O$ was attached to the manifold via a hypodermic needle and flushed and pumped three times. A syringe was used to inject 2 mL of sparged, 50 vol% H_2SO_4 into the $Na_2S \cdot 9H_2O$-containing bottle to generate H_2S. After H_2S transfer into the FeS_m-containing serum bottle, N_2 was added until pressure in the serum bottle was at only slight under-pressure relative to atmospheric pressure (~ -2.5 PSI or ~ -17 kPa). The needle holes in the serum bottle septa were covered with silicone sealant and the bottles were transferred to an oven at 40°C to allow the pyrite precipitation reaction to take place. After different, pre-determined reaction durations (between ~5

and 120 hours), the serum bottle reaction vessels were removed from the oven and frozen to stop the reaction.

Once frozen, the serum bottles were unsealed under flushing N_2 and excess H_2S in the headspace was removed. The bottles were then re-stoppered, the stoppers pierced with a hypodermic needle under flushing N_2, and the bottles left in the freeze-dryer for a day. The freeze-dried serum bottles were transferred to the anoxic chamber, and 2 mL sparged water and a few drops of the Ti^{3+} citrate were added to poise the Eh at low negative values to prevent FeS_m oxidation and ensure full dissolution of FeS_m following a previously established preferential dissolution protocol (*14*, *41*) . The serum bottles were resealed and moved to a fume hood for preferential dissolution. In the fume hood, 20 mL of sparged 1.2 M HCl was injected into the serum bottle via hypodermic syringe to fully dissolve only FeS_m and MOPS salt. Remaining solids, essentially pyrite, were separated by filtering on a 0.45 μm Millipore filter, and rinsing with sparged water. The FeS_m in HCl solutions were adjusted to 50 mL by addition of water and a 10 mL (20%) cut was dried down in clean Savillex Teflon beakers for transport and isotopic analysis. Pyrite was dissolved with drops of concentrated HNO_3, solutions were adjusted to 50 mL by addition of water and a 10 mL (20%) cut was dried down in clean Savillex Teflon beakers for transport and isotopic analysis. A 20 mL cut was taken for pyrite samples SB5 Py and SB6 Py, which were produced over short (4.66 hours) duration experiments and for which low pyrite iron yields were anticipated. In the Origins Laboratory at the University of Chicago, samples were dissolved in Aqua Regia with drops of 11 M $HClO_4$ at 140°C, and dried down twice, then treated three times with 2 mL of H_2O_2 to remove organic carbon salts left in the FeS_m solutions by MOPS. The solutions were then re-dissolved in 5 mL 6 M HCl for iron purification. A small aliquot of each solution was dried down and redissolved in 0.3 M HNO_3 to check for iron concentration of these solutions using MC-ICP-MS and determine the correct amount of volume of each sample solution to be passed through iron purification.

Analytical methods

Analytical procedures for iron purification and isotopic measurements followed standard procedures used at the Origins Laboratory of The University of Chicago (*22*, *25*, *26*, *42*, *43*). Samples were prepared from powders of black shale and IF materials, and hand-picked pyrite grains. Sample masses ranged between 12-22, 2-6, and 13-84 mg for black shale, IF, and pyrite grains, respectively. Samples were digested in clean Savillex Teflon beakers. First, 1 ml of 28 M HF + 0.5 ml of 15 M HNO_3 + a few drops of 11 M $HClO_4$ was added, and closed beakers were heated at 130ºC. Samples were evaporated to dryness and re-dissolved in Aqua Regia (0.75 ml of 11 M HCl + 0.25 ml of 15 M HNO_3) and a few drops of 11 M $HClO_4$, before heating and evaporation was repeated. The Aqua Regia + $HClO_4$ step was repeated 3 times to release all iron to solution. Samples were evaporated to dryness and 0.5 ml of 6 M HCl or 10 M HCl was added, depending on the purification procedure to be used. Larger volumes of the same acid were used for digestion of pyrite grains, which contained greater masses of Fe. Iron purification made use of both the standard 'short column' procedure, which is now routinely used in the Origins Laboratory (*42*, *43*), and a 'long column' procedure designed to more effectively eliminate Cu from the matrix (*25*, *26*), which was a potential concern for sulfide samples.

Short-column iron purification: Disposable Bio-Rad Poly-Prep polyethylene columns were filled with 1 ml of AG1-X8 200-400 mesh Cl-form anion exchange resin. The resin was pre-conditioned with 10 ml of MilliQ H_2O, 5 ml of 1 M HNO_3, 10 ml of MilliQ H_2O, 9 ml of 0.4 M HCl, 5 ml of MilliQ H_2O, and 2 ml of 6 N HCl. Samples were loaded onto columns in 0.25 ml of 6 M HCl. Matrix and interfering elements were eliminated by passing 8 ml of 6 M HCl through

the column. Iron was eluted with 9 ml of 0.4 M HCl and recovered in clean Teflon beakers. Samples were evaporated to dryness and re-dissolved in 0.25 ml of 6 M HCl, before repeating the column procedure a second time with new resin. All experimentally synthesized pyrite and FeS_m samples were also purified using this procedure.

Long-column iron purification: This alternative iron purification procedure was used to eliminate Cu as a potentially significant matrix element associated with natural sulfide phases. Reusable 30 ml Savillex Teflon columns with a 0.64 cm ID cut to 10.5 cm length were loaded with 3 ml of AG1-X8 anion exchange resin. The resin was preconditioned with 10 ml of MilliQ H_2O, 10 ml of 0.4 M HCl, 5 ml of MilliQ H_2O, 10 ml of 0.4 M HCl, and 4 ml of 10 M HCl. Samples were loaded onto columns in 0.25 ml of 10 M HCl. Matrix and interfering elements were eliminated by passing 4.5 ml of 10 M HCl, and 30 ml of 4 M HCl, the latter to eliminate Cu. Iron was eluted with 9 ml of 0.4 M HCl and recovered in clean Teflon beakers. Samples were evaporated to dryness and re-dissolved in 0.25 ml of 10 M HCl before repeating the column procedure with new resin.

Iron isotopic compositions were measured on a Neptune MC-ICPMS at the University of Chicago. Analyses were made of the extent of isotopic fractionation (δ' values), and the departure from a reference mass-dependent fractionation law (ϵ'). The Fe isotopes at masses 54, 56, 57, and 58 were measured simultaneously along with ^{53}Cr and ^{60}Ni for correction of ^{54}Cr and ^{58}Ni interferences on ^{54}Fe and ^{58}Fe, respectively. The ^{53}Cr and ^{60}Ni interferences were corrected for using the exponential law. All the Fe isotopes have molecular interferences with argide ions ($^{40}Ar^{14}N^+$, $^{40}Ar^{16}O^+$, $^{40}Ar^{16}O^1H^+$, and $^{40}Ar^{18}O^+$), which present a significant hindrance to obtaining the requisite precision to resolve mass-dependent fractionation laws. Therefore, measurements were made on the flat-topped peak shoulder in high-resolution mode using a standard Neptune entrance slit. A few analyses were done at ultra-high resolution using a Thermo Element 2 slit. Results were consistent with those obtained using the standard HR method, but offered no improvement in precision while requiring higher iron concentrations to obtain the same signal. Nickel or aluminum sampler and H skimmer cones were used. Standard-sample bracketing was used to correct isotopic ratio measurements for instrumental mass fractionation, and Fe isotopic ratios of samples are reported relative to the average isotopic ratios of the bracketing standard solutions of IRMM-524, which has an identical Fe isotopic composition to IRMM-014. The exponential law was initially used to calculate ϵ values by fixing $^{57}Fe/^{54}Fe_{std}$ to 0.362549, the value of IRMM-014. The δ and ϵ values of samples are given by:

$$\delta = \left[\left(^{i}Fe/^{54}Fe\right)_{sample}/\left(^{i}Fe/^{54}Fe\right)_{std} - 1\right] \times 10^3, \quad \text{(S1)}$$

$$\epsilon = \left[\left(^{i}Fe/^{54}Fe\right)^{*}_{sample}/\left(^{i}Fe/^{54}Fe\right)^{*}_{std} - 1\right] \times 10^4, \quad \text{(S2)}$$

and the logarithmic forms, δ' and ϵ', are given by:

$$\delta' = \ln\left[\left(^{i}Fe/^{54}Fe\right)_{sample}/\left(^{i}Fe/^{54}Fe\right)_{std}\right] \times 10^3, \quad \text{(S3)}$$

$$\epsilon' = \ln\left[\left(^{i}Fe/^{54}Fe\right)^{*}_{sample}/\left(^{i}Fe/^{54}Fe\right)^{*}_{std}\right] \times 10^4, \quad \text{(S4)}$$

where i = 56, 57, or 58 and the * indicates that ratios were corrected for mass fractionation by internal normalization to a fixed reference $^{57}Fe/^{54}Fe$ ratio using the exponential law (*17*, *20*) with $\theta^{56/57} = \ln\left(m_{i_{Fe}}/m_{54_{Fe}}\right)/\ln\left(m_{56_{Fe}}/m_{54_{Fe}}\right) = 0.672$, using the following equation,

$$\ln\left(^{i}Fe/^{54}Fe\right)^{*}_{\text{sample, corrected}} = \ln\left(^{i}Fe/^{54}Fe\right)_{\text{sample, measured}} - \ln\frac{\left(^{57}Fe/^{54}Fe\right)_{\text{sample, measured}}}{\left(^{57}Fe/^{54}Fe\right)_{\text{fixed reference}}}\frac{\ln\left(m_{i_{Fe}}/m_{54_{Fe}}\right)}{\ln\left(m_{57_{Fe}}/m_{54_{Fe}}\right)}. \quad \text{(S5)}$$

Bracketing standards were also internally normalized using the same exponential law. The bracketing standards were solutions of IRMM-524, which has the same isotopic composition as IRMM-014.

Subsequent to measurements, data were renormalized to the high-temperature equilibrium limit law running through IRMM-014 with $\theta^{56/57} = 0.678$, for display on Figs. 1B, 2B, 2C, 2D, and S6, consistent with the common convention used with other isotopic systems (*e.g. 21*, *37*, *38*). The renormalization of ϵ'^{56} values was done using

$$\epsilon'_{\text{high-T eq}} = \epsilon'_{\text{exp}} - 10 \times (0.678 - 0.672) \times \Delta\delta'^{57}Fe. \quad \text{(S6)}$$

Both the data normalized to the exponential law and to the high-temperature equilibrium limit law are presented in Tables S1 and S2, and a version of Figure 1B using normalization to the exponential law is shown on Figure S1.

Samples and standards were measured in 0.3 M HNO_3 and introduced into the plasma torch using a Cetac Aridus II or ESI Apex Omega desolvating nebulizer system with no auxiliary N_2 flow. On-peak zero was determined at the start of each measurement sequence by analyzing a clean aliquot of the same HNO_3 in which samples were measured. Sample and standard concentrations between 5 and 30 ppm were used in different measurement sessions depending on sensitivity and the mass-resolution slit being used, but most analyses made use of 10-12 ppm iron in sample and standard solutions. Measurements were made with the use of bracketing standards matched to sample concentrations within ± 5 %. Measurements of ^{56}Fe were made on a 10^{10} Ω amplifier resistor because signal intensities were generally higher than 50 V, and 10^{11} Ω amplifier resistors were used for measurement of ^{54}Cr, ^{54}Fe, ^{57}Fe, ^{58}Fe, and ^{60}Ni.

For experimentally synthesized samples, the Fe isotopic fractionation ($\delta'^{56}Fe$) was also determined by standard Fe isotopic analytical methods. A quartz cyclonic spray chamber was used to introduce 1 ppm solutions into the Neptune operating in medium-resolution mode, resulting in a signal of ~7 V. Isotopic compositions were determined by standard-sample bracketing. All Fe isotopic analyses of experimentally synthesized samples (both triple isotopic and conventional) were bracketed and normalized to IRMM-524 during analysis. The average fractionation factor we determined for the pyrite precipitation reaction was $\alpha^{56}_{\text{FeS-pyrite}} = 1.0023 \pm 0.0003$ (95% C.I.) (Fig. S2), consistent with the results of Guilbaud et al. (2011) who obtained a value of 1.0022 ± 0.0007 (*14*). This fractionation factor was determined by calculating the average difference between the FeS_m and pyrite splits from each serum bottle experiment. The degree of pyritization (the fraction of the total Fe in the pyrite pool) was calculated from the total iron masses in each split indicated by concentration measurements and known dilution factors. The low degree of pyritization values (maximum ~14 %) obtained in our experiments were not conducive to fitting the data to a Rayleigh distillation trend, however the difference between linear trends plotted

through $\delta'^{56}Fe$ *vs.* degree of pyritization for the FeS_m and pyrite data also gave an average fractionation factor of $\alpha^{56}_{FeS\text{-}pyrite} = 1.0023$ (Fig. S2).

We saw no systematic difference between short- and long-column purification techniques in triple-Fe-isotopic data for IF sample JD-C165A, and pyrite sample SF-1 599.8 Py, which were each processed multiple times using either column procedure to check the reproducibility of our measurements in the absence of geostandard materials that have been analyzed to this level of precision (Fig. S3). In all cases, the individual analyses for the pyrite sample had $\epsilon'^{56}Fe$ values that were significantly more positive than the value anticipated for IF with the same $\Delta\delta'^{57}Fe$ value (Fig. S3). In addition, as a check for possible matrix effects in the preparation of IF and pyrite samples, we performed a matrix test with IRMM-524 standard iron solution. Briefly, aliquots of an IF sample (REX 187.5) and a pyrite sample (SF-1 623.6 Py) were passed through the short-column purification procedure and the eluted matrix from each was collected. These matrix cuts were further purified by passing them through this column chemistry procedure again. The matrix cuts were mixed with a solution of IRMM-524 containing the same amount of iron as originally present in the sample aliquots, and the iron was purified with two passes on short columns in the same manner as other samples. The $\epsilon'^{56}Fe$ values of both matrix-adjusted solutions and a pure solution of IRMM-524 were all within error of zero and all identical within error (Fig. S3), suggesting that sample matrix did not systematically affect our $\epsilon'^{56}Fe$ analyses.

Modeling methods - Calculation of oxic and sulfidic sink sizes

Triple-Fe-isotopic systematics allows the isotopic composition of any low-$\delta'^{57}Fe$ pyrite to be broken into contributions from KIE during pyrite precipitation and the isotopic fractionation resulting from the removal of isotopically heavy Fe^{3+} oxyhydroxides. Because MFLs are straight lines in $\epsilon'^{56}Fe$ *vs.* $\Delta\delta'^{57}Fe$ space, the contributions of the two fractionating processes can be determined by solving for the intersection of two straight line equations (shown schematically in Fig. S5), or as shown below, by solving a pair of simultaneous equations.

For each individual pyrite, the two unknowns are the $\epsilon'^{56}Fe$ value and the $\Delta\delta'^{57}Fe$ of the Fe^{2+} pool from which pyrite formed ($\delta'^{56}Fe_w$ in the main text). We denote these two unknowns $\epsilon'^{56}Fe_w$ and $\Delta\delta'^{57}Fe_w$. In the context of the two-stage model described here and in the main text, we have the two following constraints: (1) the parcel of seawater that experienced iron oxide removal must be on the empirical MFL defined by iron formation, and (2) the line that ties a pyrite sample to the seawater parcel from which is formed must define a slope identical to the MFL for pyritization. The two equations relating $\epsilon'^{56}Fe_w$ and $\Delta\delta'^{57}Fe_w$ are:

$$\epsilon'^{56}Fe_w = a_{ox}\Delta\delta'^{57}Fe_w + b_{ox}, \quad \text{(S7)}$$

$$\frac{\epsilon'^{56}Fe_{py} - \epsilon'^{56}Fe_w}{\Delta\delta'^{57}Fe_{py} - \Delta\delta'^{57}Fe_w} = a_{KIE}, \quad \text{(S8)}$$

where a_{ox}, b_{ox}, and a_{KIE} are the known empirical values from our measurements of endmember MFLs, and $\Delta\delta'^{57}Fe$ are taken as fractionations relative to IRMM-014. These two equations can be solved for the two unknowns and we have,

$$\Delta\delta'^{57}Fe_w = \frac{(\epsilon'^{56}Fe_{py} - a_{KIE}\Delta\delta'^{57}Fe_{py} - b_{ox})}{(a_{ox} - a_{KIE})}, \quad \text{(S9)}$$

$$\epsilon'^{56}Fe_w = a_{ox}\frac{(\epsilon'^{56}Fe_{py} - a_{KIE}\Delta\delta'^{57}Fe_{py} - b_{ox})}{(a_{ox} - a_{KIE})} + b_{ox}. \quad \text{(S10)}$$

Note that $\Delta\delta'^{57}Fe_w \sim 1.5\times \Delta\delta'^{56}Fe_w$ where $\delta'^{56}Fe_w$ values are discussed in the main text. The extent of Fe^{2+} oxidation (F_{ox}) to give a certain $\Delta\delta'^{57}Fe_w$ was calculated using a Rayleigh distillation model:

$$\Delta\delta'^{57}Fe_w = \Delta\delta'^{57}Fe_i + 1000(\alpha - 1)\ln(1 - F_{ox}), \qquad \text{(S11)}$$

where α is the fractionation factor during Fe^{2+} oxidation and precipitation that gives a fractionation $1000\times(\alpha^{56}-1) = 1‰$ [$(\alpha^{57}-1)\sim 1.5\times(\alpha^{56}-1)$] during Fe^{3+} oxyhydroxide removal (*16*), the subscript $_i$ denotes the starting $\Delta\delta'^{57}Fe$ value for a hydrothermal Fe^{2+} source of approximately -0.3 ‰ (*46*), assumed to be on the empirical MFL defined by iron formations.

The fraction of pyrite precipitated (f_{py} in the main text) was also determined with a Rayleigh distillation model. In this case, the measured fractionation was taken to reflect the cumulative product of pyrite precipitation from a dissolved Fe^{2+} reservoir with initial $\Delta\delta'^{57}Fe$ value of $\Delta\delta'^{57}Fe_w$. This contrasts with how one might consider *in situ* measurements of individual nodule layers, because those better approximate instantaneous precipitate compositions during the growth of pyrite grains (*17*, *18*). The magnitude of the KIE that was expressed in the product was calculated as the difference between the product and initial reactant:

$$\Delta\delta'^{57}Fe_{py} - \Delta\delta'^{57}Fe_w = \frac{(f_{py} - 1)\times 1000(\alpha^{57} - 1)\ln(1 - f_{py})}{f_{py}}, \qquad \text{(S12)}$$

where we assumed the maximum fractionation for pyrite precipitation (via FeS_m) from Fe^{2+} of $1000\times(\alpha^{56}-1) = -3.1‰$ [$(\alpha^{57}-1) \sim 1.5\times(\alpha^{56}-1)$] suggested by ref. (*14*). The value of f_{py} was determined by solving this transcendental equation numerically. The fractional size of the sulfidic sink, F_{py}, witnessed by each pyrite, was calculated as,

$$F_{py} = f_{py}\times(1 - F_{ox}). \qquad \text{(S13)}$$

An uncertainty not considered in calculating f_{py} is the effect of isotopic exchange between freshly precipitated pyrite and ambient Fe^{2+}. A recent experimental study (*47*) provided some evidence that the growing surface of freshly precipitated microscopic pyrite grains may undergo isotopic equilibration with the ambient Fe^{2+} pool. Because the anticipated equilibrium fractionation factor for pyrite formation is large and positive (*48*), such a process could partially offset large kinetic isotope effects enriching pyrite in light Fe isotopes, resulting in a smaller net fractionation between pyrite and Fe^{2+} at a given F_{py}. In practice, however, isotopic re-equilibration of pyrite has been observed only at elevated temperatures (80°C), and where the surface area to volume ratio of microscopic pyrites allows this surface exchange effect to exert a significant control on the bulk Fe isotopic composition. This process should become diminishingly important at lower temperatures, as observed in experiments (*14*) and nature (*15*), and as pyrite grains grow larger than 10 μm, and certainly as they reach macroscopic sizes like the diagenetic nodules studied here. While the required kinetic data on pyrite growth and isotopic exchange rates are not currently available to model this process accurately at appropriate low-temperature marine conditions, it is unlikely that isotopic re-equilibration of pyrite was a major control on the bulk Fe isotopic composition of diagenetic pyrites.

In practice, all the parameters $\epsilon'^{56}Fe_{py}$, $\Delta\delta'^{57}Fe_{py}$, a_{ox}, b_{ox}, and a_{KIE} have analytical uncertainties associated with them. The effects of these errors on estimates of fractional iron sinks were propagated using a Monte Carlo method implemented in MATLAB. For each pyrite and IF datapoint, an array of simulated datapoints was generated by randomly sampling 1000 times from a normal distribution defined by the reported 95 % C.I. of the measured $\epsilon'^{56}Fe$ and $\delta'^{57}Fe$ values (Table S1). From the 1000 sets of randomly generated IF datapoints, 1000 MFLs were generated by linear regression to encompass the anticipated range of seawater Fe^{2+} evolutions in $\epsilon'^{56}Fe$ *vs.* $\Delta\delta'^{57}Fe$ space that could be driven by Fe^{3+} oxyhydroxide precipitation. An array of 1000 values for the kinetic slope was generated by randomly sampling 1000 times from a normal distribution defined by the 95 % C.I. of the experimentally determined slope. We then solved the 1000 resulting simultaneous equations 1000 times for the randomly generated datasets using the approach described above. Certain output values from the random resampling had to be rejected, as they did not allow for solving for F_{ox} and f_{py} values using the Rayleigh distillation equations. These cases were where: (*i*) the required fractionation during pyritization ($\Delta\delta'^{57}Fe_{py}$ - $\Delta\delta'^{57}Fe_w$) was larger in magnitude than the maximum instantaneous fractionation for pyrite precipitation from Fe^{2+} (via FeS_m) with $1000\times(\alpha^{56}\text{-}1) = -3.1‰$ [$(\alpha^{57}\text{-}1) \sim 1.5\times(\alpha^{56}\text{-}1)$] (*14*)); (*ii*) the randomly generated data placed a pyrite datapoint below the IF line in $\epsilon'^{56}Fe$ *vs.* $\Delta\delta'^{57}Fe$ space, thus requiring a positive $\Delta\delta'^{57}Fe$ offset of the pyrite from the IF line; and (*iii*) where the randomly generated data required an intercept between the IF and KIE lines at a $\Delta\delta'^{57}Fe_w$ value more positive than the assumed hydrothermal Fe^{2+} source $\Delta\delta'^{57}Fe$ value of approximately -0.3‰ (*46*). The probability distributions for F_{ox} and F_{py} from the Monte Carlo simulation are shown in Fig. 3 and Table S5, and we also used central estimates of F_{ox} and F_{py} from the Monte Carlo simulations to calculate the O_2 yields given in Fig. 3 and Table S5. Monte Carlo simulation estimates of f_{py} and F_{ox} for each pyrite sample span a large range, but these variations are strongly correlated. This is because a more negative estimate for the isotopic composition of seawater $\Delta\delta'^{57}Fe_w$ (which implies a larger F_{ox}), gives a smaller estimate for the fractionation during precipitation of pyrite from the oceanic iron pool (which implies a larger f_{py}). These two effects have an opposite impact on the estimate of F_{py}, therefore, F_{py} estimates vary less than F_{ox} and f_{py}.

As an alternative to a Rayleigh distillation describing upward large scale advection of Fe^{2+}-rich deep waters (*e.g. 49–52*), we also explored the possibility that the isotopic evolution of the Fe^{2+} reservoir during removal of Fe^{3+} oxyhydroxides to the oxic Fe sink was controlled by steady-state eddy diffusion of Fe^{2+} from deep waters, and O_2 from the photic zone, following the model of Czaja *et al.* (2012) (*34*). We developed a model to replicate its salient features, using a finite difference approach. In the model, a photic zone with a fixed O_2 level overlies a basin that contains anoxic, Fe^{2+}-rich water at depth. Dissolved O_2 is transported downward, and Fe^{2+} upward, by eddy diffusion, and $Fe(OH)_3$ precipitates where these species meet, following second-order reaction kinetics with temperature and salinity-dependent rates calculated after ref. (*53*). Precipitation rates peak in a narrow reaction zone, around which both dissolved species' concentrations decrease to near zero levels. Precipitated $Fe(OH)_3$ is removed from the column with a first-order rate constant of 0.79 day^{-1}. The Fe^{2+} oxidation reaction (which consumes Fe^{2+} and O_2) follows a second-order kinetic rate law that is dependent on temperature, salinity, and pH. This parameter space was explored extensively by ref. (*34*) and we simply followed their preferred input parameters in order to replicate their model. In the model, the equilibrium fractionation for Fe^{2+}-Fe^{3+} isotopic exchange was implemented by treating ^{56}Fe and ^{54}Fe as separate species and scaling the reaction rate constants according to the relevant fractionation factor. No fractionation factor was applied to the eddy diffusion process. In the model, the majority of Fe oxidation takes place within the narrow

reaction zone, and it is there that significant Fe isotopic fractionations are developed in the Fe^{2+} reservoir in a steady-state distillation process.

A list of input parameters for different model runs is provided in Table S4. For simplicity, in contrast to (*34*), we employed a fixed concentration rather than a fixed production rate boundary condition for O_2. The fixed concentration we chose matches the steady-state O_2 level at the base of the photic zone in ref. (*34*)'s model. Our results (Fig. S8) replicate theirs, so this simplification of the boundary condition does not affect the model output.

It can be shown with a simple scaling argument that the steady state reaction zone develops at the location where eddy diffusive transport of O_2 downwards, and Fe^{2+} upwards, lead to concentrations of O_2 and Fe^{2+} in a 1:4 ratio, the stoichiometry required for complete titration of dissolved Fe^{2+} by O_2-mediated oxidation. Consider a water column with 5 levels: Level 1 – ocean surface; Level 2, photic zone base; Level 3 – top of reaction zone; Level 4 – base of reaction zone; and Level 5 – base of model basin (Fig. S8). The diffusive fluxes, J_{O2} and J_{Fe2+}, are given approximately by,

$$J_{O2} = D[O_2]_2/z_{2\text{-}3}, \quad \text{(S14)}$$

$$J_{Fe2+} = D[Fe^{2+}]_5/z_{5\text{-}4}, \quad \text{(S15)}$$

where D is the eddy diffusivity (0.1 cm^2s^{-1}), and $z_{i\text{-}j}$ is the depth difference between level i and level j, and the subscripts on the concentrations indicate concentrations at the fixed boundary conditions for O_2 at the top of of the model, and Fe^{2+} at the base of the model. In the reaction zone, Fe^{2+} is quantitatively oxidized by O_2, in a 4:1 stoichiometry, which gives the approximation $J_{O2} \approx \frac{1}{4} J_{Fe2+}$ at this depth. Rearranging for $z_{5\text{-}4}$ gives:

$$z_{5\text{-}4} \approx (z_{2\text{-}3}[Fe^{2+}]_5)/(4[O_2]_2). \quad \text{(S16)}$$

Recognizing that $z_{5\text{-}2} = z_{5\text{-}4} + z_{2\text{-}3}$ for the case where the reaction zone is ultimately thin, and substituting appropriately gives:

$$z_{5\text{-}4} \approx z_{5\text{-}2}/(1+(4[O_2]_2/[Fe^{2+}]_5)), \quad \text{(S17)}$$

and thus, the depth of the reaction zone can be calculated. This depth level is plotted in Figure S8 and agrees well with the depth level in the numerical model where the peak in $Fe(OH)_3$ is located. This comparison and the fact that we can reproduce the profiles calculated by ref. (*34*) validates our numerical code.

In the dispersion reaction model, the calculation of F_{ox} is less straightforward than in the Rayleigh distillation because there is no provision for Fe removal as pyrite. In the context of an upward Fe^{2+} supply, F_{ox} at a given depth was calculated by integrating the steady-state Fe^{2+} oxidation rate from the bottom of the model upward to that depth, and dividing this value by the Fe^{2+} oxidation rate integrated over the entire water column.

We plotted $\delta^{56}Fe_{Fe2+}$ *vs.* $\ln(1\text{-}F_{ox})$ from this model in Fig. S9, for different values of the fractionation factor between Fe^{2+} and $Fe(OH)_3$. A feature of these model runs is that a small, but significant negative isotopic fractionation is imparted to $\delta^{56}Fe_{Fe2+}$ before it reaches the reaction zone, whilst F_{ox} is still very close to zero. This fractionation can be understood as resulting from diffusion. The Fe^{2+} input at the base of the model region has a fixed $^{56}Fe/^{54}Fe$, but due to

preferential removal of ^{56}Fe in the reaction zone, the ratio of concentration gradients is fractionated relative to the input $^{56}Fe/^{54}Fe$ ratio, with a relatively steeper concentration gradient for ^{56}Fe. As a result, ^{56}Fe diffuses slightly faster into the reaction zone, leaving the column underlying the reaction zone with a slightly lower $^{56}Fe/^{54}Fe$. This is expressed in the slightly negative $\delta^{56}Fe_{Fe2+}$ already established at the base of the reaction zone before Fe^{2+} oxidation begins to dominate the isotopic evolution.

Once within the reaction zone, $\delta^{56}Fe_{Fe2+}$ evolves linearly versus $\ln(1-F_{ox})$, becoming increasingly negative as F_{ox} increases, so this evolution is functionally very similar to a Rayleigh distillation. However, for a given input isotopic fractionation factor α^{56} between Fe^{2+} and $Fe(OH)_3$, the slope of $\delta^{56}Fe_{Fe2+}$ vs. $\ln(1-F_{ox})$ is $\sim 0.39 \times (\alpha^{56} - 1) \times 1000$, while an upwelling modelled using a Rayleigh distillation would yield a correlation of slope $(\alpha^{56} - 1) \times 1000$. As such, reaching a given negative value of $\delta^{56}Fe_{Fe2+}$ would require a larger F_{ox} at the same value of α^{56}, or vice versa, in the dispersion-reaction model versus a Rayleigh distillation. This effect is partially offset, particularly at lower F_{ox} values, by the initial depletion in $\delta^{56}Fe_{Fe2+}$ caused by eddy diffusion in the underlying water column.

F_{ox} and F_{ox}/F_{py} were recalculated using the evolution described by model outputs in order to compare to results from the model using Rayleigh distillation (Fig. S10). Dispersion-reaction modeling conducted with an input value for α^{56} of 1.001 as used in our Rayleigh model, or 1.004 as used in ref. (*34*). Using $\alpha^{56} = 1.001$ in the dispersion-reaction model gives higher F_{ox} values than in our Rayleigh distillation modeling. All pyrite triple Fe isotope compositions still lie at $F_{ox}/Fe_{py} < 10$ (allowing positive O_2 fluxes in certain scenarios) but the error bars would also allow marginal cases with higher F_{ox}/Fe_{py} (Fig. S10). However, the same model would require $[Fe^{2+}]$ to be depleted by partial oxidation by a factor of several hundreds in order to explain the lowest recorded $\delta^{56}Fe_{IF}$ values, and it is unclear whether such extreme Fe^{2+} depletions would still allow the deposition of Fe-rich chemical sediments at all. This suggests that the use of such a small α^{56} value might not appropriate in the context of this model, and why the larger fractionation factor was employed in previous iterations of the model (*34*). That larger fractionation factor yields low F_{ox}/F_{py} consistent with pyrite burial being a net oxygen source (Fig. S10).

Sample Materials

Geological setting and age constraints for shale-hosted pyrite are given by Rouxel et al. (2005) (*9*). Ages and stratigraphic positions for all samples used in this study are provided in Table S3. References to age constraints for pyrite and shale samples, and most IF samples, are provided in refs. (*9*, *10*, *30*). Ages for the Hotazel Formation and Isua Supracrustal Belt IFs are from ref. (*2*) and ref. (*54*), respectively, and the geologic setting and Fe isotopic systematics of these IF have been discussed in the literature elsewhere (*28*, *55*, *56*).

Pyrite grains from organic-rich shales as well as a few whole-rock organic-rich shale and IF samples were selected for this study. Pyrite grains and whole-rock shale samples were selected from a set of drill core samples previously studied for Fe isotopic variations by refs. (*9*, *30*). New pyrite grains were picked at the University of Hawaii. The nature of these grains was described in detail by ref.(*6*). Pyrite in organic-rich shales that were subsampled in our study occur as nodules ~ 1 mm to 1 cm in diameter, with C-rich inclusions in variable amounts. The nodular pyrite either had no internal texture, or was composed of concentrically laminated, fine-grained pyrite or bladed pyrite crystals. Euhedral pyrite crystals commonly overgrew the outer part of the nodules. Shale laminae typically bend around pyrite nodules, which supports interpretation of their origin as being formed early on during diagenesis. Pyrite nodules often display complex features such as multiple-

growth bands or composite nodules formed by coalescence of several nodules. Dissolution and reprecipitation of early diagenetic sulfide crystals and nodules could have happened in some samples and likely resulted in formation of massive, pre-compactional pyrite, often characterized by euhedral grains free of C-rich inclusions.

Localized dissolution-reprecipitation is unlikely to have affected Fe-isotopic compositions of pyrites. In the large sets of samples analyzed per formation by ref. (*9*), strongly negative δ^{56}Fe values were a consistent feature, and no relationship between Fe isotopic composition and the nature of individual pyrite grains was reported, which supports the notion that these are primary sedimentary signatures and not the results of later alteration of the host rocks. The fidelity of the pyrite Fe isotope record as an archive of primary sedimentary signatures was recently discussed by ref. (*11*). In brief, the resistance of this system to metamorphic overprinting due to the high abundance of Fe, low solubility of pyrite, and small size of Fe isotopic fractionations at metamorphic temperatures all make it unlikely that primary sedimentary Fe isotopic signatures have been compromised by secondary processes that may nonetheless have affected the texture of pyrite grains. It was recently demonstrated through *in situ* work that Archean pyrites that experienced late fluid circulation, which led to partial recrystallization and alteration of S isotopic systematics, did not modify the Fe isotopic composition (*18*), in line with our expectations outlined above.

Supplementary Text

Background on mass fractionation laws for Fe isotopes

Instantaneous fractionations

Numerous reaction pathways have been proposed to create the >5‰ δ^{56}Fe range in Archean IFs, shales, and pyrites. The extent of Fe isotopic fractionation is insufficient to discriminate between different scenarios for sedimentary iron cycling in the Archean oceans, because several fractionation processes can generate a large and indistinguishable range in delta values. Considering two isotopic ratios can resolve this ambiguity for sedimentary pyrite, because different processes impart isotopic fractionations that follow different slopes in δ^{56}Fe *vs.* δ^{57}Fe space corresponding to mass fractionation laws (MFL). Mass-dependent fractionation is described with a power law:

$$\alpha^{56}{}_{A/B} = \alpha^{57}{}_{A/B}{}^{\theta^{56/57}}, \qquad \text{(S18)}$$

where $\alpha^{x}{}_{A/B}$ are fractionation factors for isotope x between reservoirs A and B, and $^{56/57}\theta$ is the mass dependent exponent or slope in triple Fe isotope space (*20*). Natural processes imparting different slopes of MFLs in three-isotope diagrams have been identified for O (*57–60*), Mg (*19*, *61*), S (*44*, *62*, *63*), Ca (*64*), Ti (*64*), and Fe (*21*, *22*), but this has yet to be investigated for Fe isotopes in sedimentary rocks with enough precision to resolve distinct slopes. The slope $\theta^{56/57}$ for the triple-Fe-isotopic diagram is given by:

$$\theta^{56/57} = \frac{\Delta\delta'^{56}Fe}{\Delta\delta'^{57}Fe} = \frac{\ln\left[\left(\frac{^{56}Fe}{^{54}Fe}\right)_{sample}\Big/\left(\frac{^{56}Fe}{^{54}Fe}\right)_{std}\right] - \ln\left[\left(\frac{^{56}Fe}{^{54}Fe}\right)_{initial}\Big/\left(\frac{^{56}Fe}{^{54}Fe}\right)_{std}\right]}{\ln\left[\left(\frac{^{57}Fe}{^{54}Fe}\right)_{sample}\Big/\left(\frac{^{57}Fe}{^{54}Fe}\right)_{std}\right] - \ln\left[\left(\frac{^{57}Fe}{^{54}Fe}\right)_{initial}\Big/\left(\frac{^{57}Fe}{^{54}Fe}\right)_{std}\right]}, \qquad \text{(S19)}$$

where δ' is related to the standard δ notation by:

$$\delta' = 1000\times\ln[(\delta/1000)+1]. \quad \text{(S20)}$$

Slopes vary only subtly between MFLs and therefore it is convenient for the purpose of visualization to express one isotopic ratio in terms of its deviation from an arbitrary reference law in parts per 10,000 by using ϵ' notation (*20*, *22*) where:

$$\epsilon'^{56}\mathrm{Fe} = \left(\Delta\delta'^{56}\mathrm{Fe} - \theta_r^{56/57} \times \Delta\delta'^{57}\mathrm{Fe}\right)\times 10. \quad \text{(S21)}$$

In ϵ'^{56}Fe *vs.* $\Delta\delta'^{57}$Fe diagram, MFLs are straight lines, and when the high-temperature equilibrium limit law with $\theta_r^{56/57} = 0.678$ is used as the reference law, ϵ'^{56}Fe values are 0 if fractionation follows the high-temperature equilibrium limit law. Other MFLs will then have positive or negative slopes if $\theta^{56/57}$ is larger or smaller than 0.678, respectively.

These laws describe mass-dependent fractionation in a single-step process. This approach is an oversimplification in cases where isotopes have been fractionated via several geochemical pathways, or via Rayleigh distillation. These complications are well-documented in the more mature field of triple O and S isotopes (*44*, *57*, *59*, *62*, *63*) but we show here that these concerns are of diminished importance in application to low-temperature Fe isotope systematics. This is because Rayleigh distillation produces trends in ϵ'^{56}Fe *vs.* $\Delta\delta'^{57}$Fe space that are practically indistinguishable from instantaneous MFLs over the natural range of Fe isotopic variations.

Rayleigh distillation

Reactant reservoir

In the case of Rayleigh distillation, closed-system evolution of a reactant reservoir (A) during formation of a product (B) results in an observed slope in three-isotope space for A that is distinct from the intrinsic slope of the instantaneous fractionation process (Fig. S4A) (*25*, *62*). In this study, the evolution of the reactant reservoir corresponds to the generation of an isotopically light Fe^{2+} pool through the removal of an isotopically heavy Fe^{3+}-oxyhydroxide product. The evolution of the reactant, written in δ' notation, is,

$$\delta'^{x}\mathrm{Fe}_A = (\alpha^x - 1)\times\ln\left({}^{54}f_A\right)\times 1000 + \delta'^{x}\mathrm{Fe}_{A,i}, \quad \text{(S22)}$$

where $\delta'^{x}\mathrm{Fe}_{A,i}$ is the initial isotopic composition of the reactant, $\delta'^{x}\mathrm{Fe}_A$ is the isotopic composition of the reactant when a fraction f_A of the reactant A remains, and α^x is the isotopic fractionation factor for isotope x in the reaction of A to form product B.

In three-isotope space, the isotopic composition of the reactant will evolve with an effective slope, $\theta^{56/57}_{\mathrm{eff}}$,

$$\theta^{56/57}_{\mathrm{eff}} = \frac{\delta'^{56}\mathrm{Fe}_A - \delta'^{56}\mathrm{Fe}_{A,i}}{\delta'^{57}\mathrm{Fe}_A - \delta'^{57}\mathrm{Fe}_{A,i}} = \frac{(\alpha^{56}-1)\times\ln\left({}^{54}f_A\right)}{(\alpha^{57}-1)\times\ln\left({}^{54}f_A\right)} = \frac{\alpha^{57}{}^{\theta^{56/57}_{\mathrm{inst}}}-1}{\alpha^{57}-1}, \quad \text{(S23)}$$

where $\theta^{56/57}_{\mathrm{inst}}$ is the intrinsic slope for the instantaneous reaction.

Distinction between θ_{inst} and θ_{eff} is significant in the O and S isotope systems, where fractionations and relative isotopic mass differences are large. In the case of Fe isotopes, specifically Rayleigh distillation of aqueous Fe^{2+} driven by oxidation and removal of Fe^{3+}

minerals, the relevant values for $\theta^{56/57}_{inst}$ and α^{57} are 0.678 and on the order of 1.0015, respectively (*14*). Using these values results in $\theta^{56/57}_{eff} \approx 0.6778$, which is smaller than the intrinsic slope by only 0.0002 and not resolvable from the intrinsic slope for any naturally occurring range of fractionations (Fig. S4A). A slightly different relation between the effective and intrinsic slopes for UV photo-oxidation, with $\alpha^{56} = 1.0012$, previously gave the same result that the effective slope for the evolving reactant reservoir was smaller than the instantaneous slope by just 0.0002, and thus the two slopes were indistinguishable within current measurement uncertainties (*22*). These calculations imply that theoretical, single-step MFLs are an appropriate approximation for the evolution in triple-Fe-isotopic space of an Fe^{2+} reservoir affected by oxidation and removal of Fe^{3+} products following a Rayleigh distillation.

Cumulative product reservoir

The cumulative product reservoir during Rayleigh distillation, which is how we treat the pyrite precipitation along the kinetic MFL, also follows a trend in triple-Fe-isotope space that is distinct from the instantaneous MFL, however in this case the evolution is not linear. The evolution of the cumulative product B is:

$$\delta'^{x}Fe_B = \left({}^{54}f_B - 1\right) \times \ln\left[\frac{\left(1 - {}^{54}f_B\right)}{{}^{54}f_B}\right] \times (\alpha^{x} - 1) \times 1000 + \delta'^{x}Fe_{A,i}, \qquad \text{(S24)}$$

where $\delta'^{x}Fe_B$ is the isotopic composition of the cumulative product when a fraction f_B (= 1- f_A) of the reactant has been consumed.

Nie *et al.* (*22*) showed that as the cumulative product reservoir grows and the reactant pool is consumed, the deviation of the cumulative product $\epsilon'^{56}Fe$ value, $\epsilon'^{56}Fe_{cumulative}$, relative to value $\epsilon'^{56}Fe_{inst}$ that is expected to fall on the instantaneous MFL at a given $\delta'^{57}Fe$ value is:

$$\epsilon'^{56}Fe_{cumulative} - \epsilon'^{56}Fe_{inst} = 10{,}000\left[\left(\theta^{56/57}_{inst} - 1\right) \times \ln\left(1 - {}^{54}f_A\right) + \ln\left(1 - {}^{54}f_A{}^{\alpha^{56}}\right) - \theta^{56/57}_{inst} \times \ln\left(1 - {}^{54}f_A{}^{\left(\alpha^{56^{1/\theta^{56/57}_{inst}}}\right)}\right)\right]. \qquad \text{(S25)}$$

Here, the relevant values for $\theta^{56/57}_{inst}$ and α^{56} are 0.6743 (derived from our triple-Fe-isotope measurements) and 0.9969 (the largest proposed Fe isotopic fractionation during pyrite precipitation from Fe^{2+} via FeS_m (*14*)), respectively. Inserting these values into S25 gives a non-linear trend shown in Fig. S4B, where the maximum deviation of the cumulative product reservoir from the instantaneous MFL is less than 0.01 $\epsilon'^{56}Fe$ units, and thus well within typical analytical errors of 0.05 (95 % C.I.). These calculations imply that theoretical, single-step MFLs are an appropriate approximation for the evolution in triple-Fe-isotopic space of cumulative product reservoir pyrite following a Rayleigh distillation.

Iron isotope MFLs

Mass-dependent triple-Fe-isotopic systematics have been explored in few publications to date, and only once previously in the context of low-temperature aqueous geochemistry. Nie *et al.* (*22*) determined $\theta^{56/57} = 0.6785 \pm 0.0009$ associated with UV photo-oxidation of dissolved Fe^{2+} in

anoxic solutions at near-neutral pH. A high precision measurement of the ca. 3.83 Ga IF-G geostandard from an IF in Isua, Greenland has $\epsilon'^{56}Fe$ and $\Delta\delta'^{57}Fe$ values consistent with isotopically heavy ferric precipitates from those experiments (*22*) and both are within error of the high-temperature limit equilibrium law with $\theta^{56/57} = 0.678$. However, the magnitude of isotopic enrichment in IF-G and isotopically heavy IF oxyhydroxides in general provide insufficient leverage in three-isotope space to distinguish different MFLs at the available precision for $\epsilon'^{56}Fe$. Whether different iron oxidation pathways for IF deposition do have distinct MFLs has not yet been tested experimentally. However, the fact that the high-temperature equilibrium law, the MFL for photo-oxidation, and our observed MFL defined by IFs including the Hotazel Mn-rich IF samples that were most likely fractionated by direct O_2 oxidation (*28*), are all within error of one another, suggests that fractionations of Fe isotopes driven by Fe^{2+}-Fe^{2+} equilibration may follow the equilibrium MFL regardless of the oxidation process involved (*66*). The empirical constraints provided by new natural samples measurements here, and the experiments of Nie *et al.* (*22*), agree with the previously documented phenomenon that the high-temperature equilibrium limit law is broadly applicable in equilibrium isotope exchange processes including some of those that occur at low temperatures (*20*). The same may be true for Fe isotopic fractionation during iron reduction processes like DIR, as it has been shown that this process introduces fractionation during Fe^{2+}-Fe^{3+} equilibration following the reduction step (*33*). It will be important for future studies to constrain the value of $\theta^{56/57}$ for the remaining proposed oxidation pathway for IF, anoxygenic photoferrotrophy (*51*, *65*). However our results to date suggest it is unlikely that triple-Fe-isotopic systematics will be able to identify the oxidation pathway for IF due to the tendency of Fe^{2+} and Fe^{3+} to rapidly isotopically equilibrate (*66*).

Precipitation of pyrite is a kinetically controlled process associated with a large kinetic isotope effect that enriches early precipitates in the light isotopes of Fe (*14*, *15*). The $\theta^{56/57}$ for kinetic processes can take a range of values depending on the specific reaction process taking place, but is in general expected to be smaller than the high-temperature equilibrium limit law $\theta^{56/57}$ value (*19*, *20*). The value of $\theta^{56/57}$ relevant to pyrite precipitation did not have an empirical constraint prior to our study. Our pyrite precipitation experiments resulted in maximum degree of pyritization of ~14% (Fig. S2). By mass balance most iron was always left in the FeS_m pool and large fractionations from the starting composition of the experiment were observed in the pyrite pool, which provides leverage to determine the slope of the instantaneous MFL associated with pyrite precipitation. Our triple-Fe-isotopic analysis is consistent with a single kinetic MFL, with a slope $\theta^{56/57}_{KIE} = 0.6743 \pm 0.0005$. This is a much shallower slope than that of the equilibrium limit law associated with redox equilibrium (*19*, *20*).

Figures

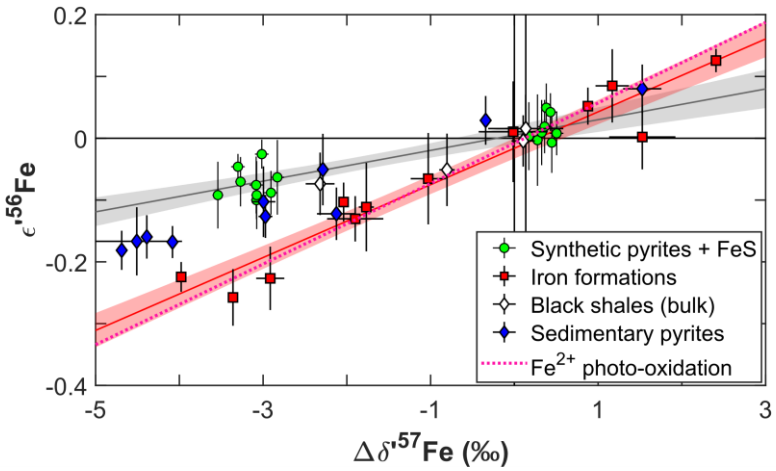

Fig. S1.
Triple-Fe-isotopic systematics for IFs, pyrites, black shales, and laboratory grown pyrite and FeS, in ϵ'^{56}Fe *vs.* $\Delta\delta'^{57}$Fe space, normalized to the exponential law (Tables S1, S2; Fig. 1A of the main text shows the same figure normalized to the high-T equilibrium MFL). $\Delta\delta'^{57}$Fe values are reported as differences from IRMM-014 and the starting material of experiments, for the natural samples and the synthetic pyrites, respectively. Error bars and envelopes are 95% confidence intervals. The slopes of end-member MFLs associated with iron-redox processes (red line and red envelope) and KIEs (black line and grey envelope) during pyritization are constrained through analysis of IFs and laboratory pyrite precipitates via the H_2S pathway (*14*, *27*, *40*), respectively. The slope of the IF MFL agrees well with the theoretical high temperature equilibrium limit law (defined by the horizontal axis, (*20*)), and an experimentally determined MFL for Fe^{2+} oxidation (via UV photo-oxidation (*22*)), implying control by Fe^{2+}-Fe^{3+} equilibrium. Synthetic pyrite and FeS define a kinetic MFL for sulfide precipitation. Pre-GOE pyrites fall in an intermediate space between redox-equilibrium and kinetic endmembers.

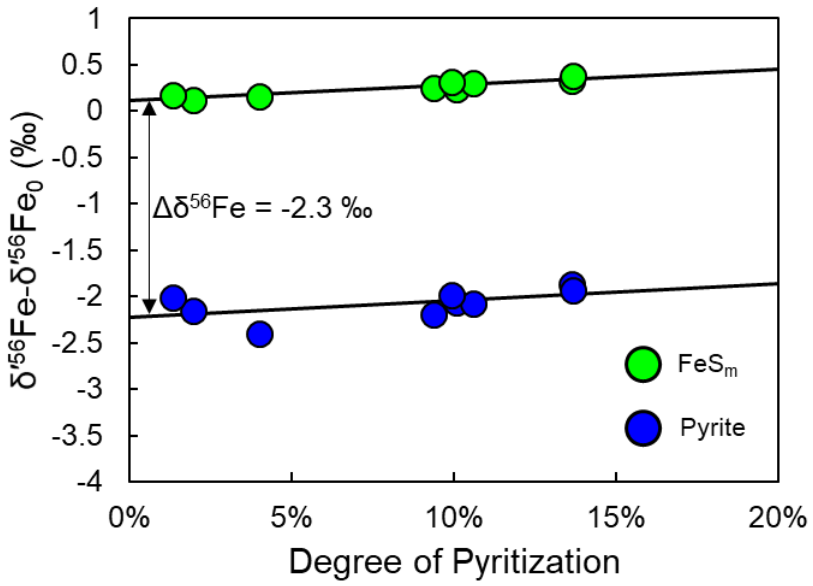

Fig. S2.

Iron isotopic fractionation between FeS_m and pyrite during abiotic precipitation of pyrite. The average Fe-isotopic fractionation between FeS_m and pyrite, a shift in $\delta'^{56}Fe$ of -2.3 ‰, is determined both through taking the average difference between the two phases in individual experiments, and through the difference between linear fit lines of $\delta^{56}Fe$ *vs.* degree of pyritization.

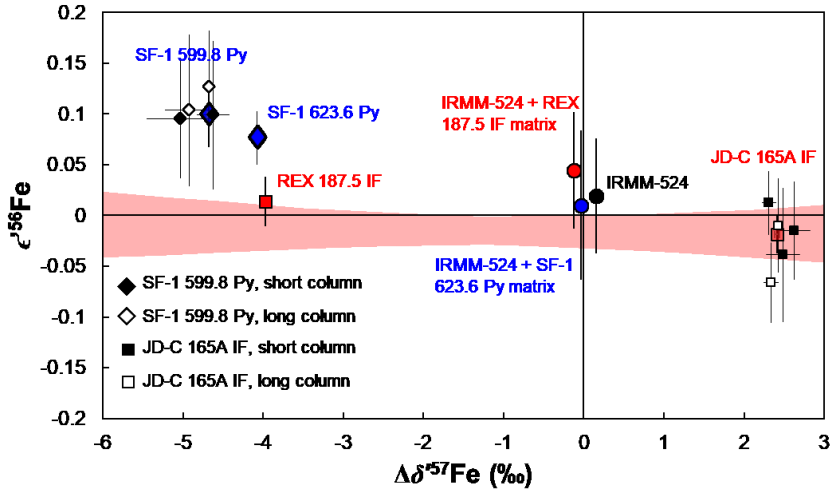

Fig. S3.

Tests performed on triple-Fe-isotopic analyses. Replicate aliquots of IF sample JD-C 165A and pyrite sample SF-1 599.8, purified using short-column (black-filled symbols) and long-column (open symbols) chromatography procedures were analyzed, with the average values for each sample shown with the pale-colored symbols in the background. Despite some analytical scatter, we see no significant or systematic effect of using one purification procedure over another, and all replicate pyrite analyses were distinct from the triple-Fe-isotopic composition one would expect for a sample that was fractionated solely by the redox processes driving the IF MFL (error enveloped of the IF MFL is shaded in red). Matrix mixing tests were performed with IRMM-524 and matrix from IF sample REX 187.5 (bold, red square) and pyrite sample SF-1 623.6 Py (bold, blue diamond). These revealed no resolvable matrix effect on ϵ'^{56}Fe analysis, with the pure IRMM-524 solution (black circle), IF matrix and IRMM-524 solution (red circle), and pyrite matrix and IRMM-524 solution (blue circle) all having ϵ'^{56}Fe values which are within error of one another and zero. Note that if matrix effects drove the difference between pyrite and IF triple-Fe-isotope variations, the IRMM-524 sample doped with pyrite matrix would have significantly more positive ϵ'^{56}Fe values than the IF-doped standard, which is not the case. $\Delta\delta'^{57}$Fe values are differences from to IRMM-014.

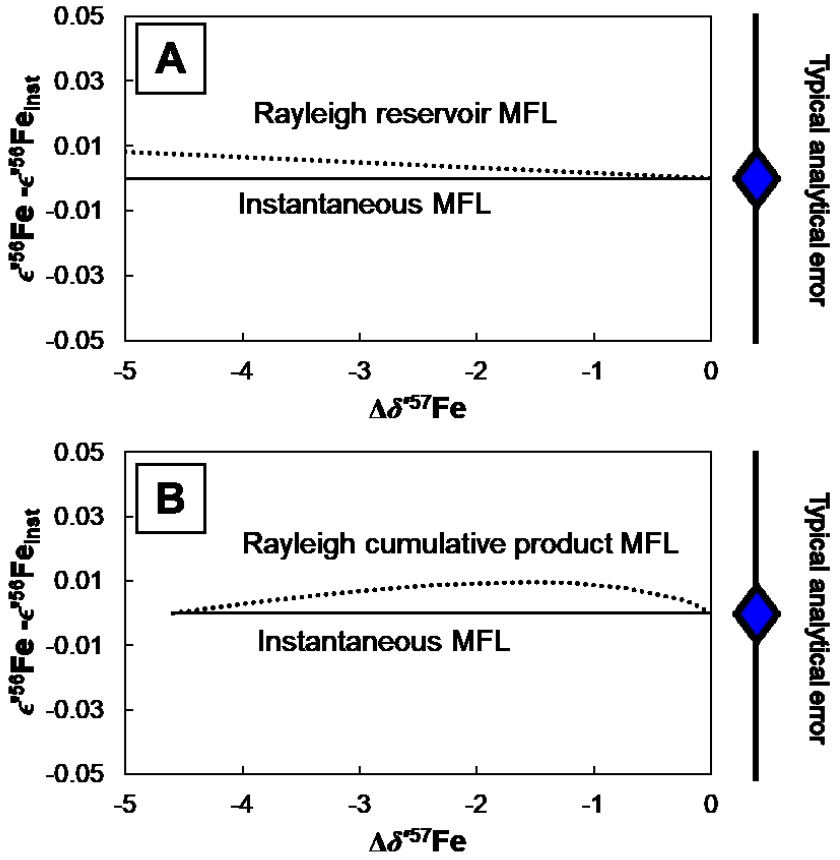

Fig. S4.

Rayleigh distillation effects in triple-Fe-isotopic space. A. Comparison of the effective MFL for Rayleigh distillation (dotted line) with the instantaneous MFL for the fractionation between reactant and product (solid line). The differing slopes result in a $\theta^{56/57}$ difference of just 0.0002, well within achievable analytical error for natural ranges of fractionation. B. Comparison of the effective mass fractionation array (dotted line) with the instantaneous MFL for the product precipitation (solid line), for the case of pyrite precipitation from solution as a cumulative Rayleigh distillation product with the maximum instantaneous fractionation $1000 \times (\alpha^{56}\text{-}1)$ of -3.1 ‰ suggested by ref. (*14*). The maximum deviation is less than 0.01 ϵ'^{56}Fe units, well within analytical error. Both reactant and product reservoir trends are identical to the instantaneous MFL for the process driving Fe isotopic fractionation over the naturally observed range of values within analytical error for ϵ'^{56}Fe value, which is typically on the order of ±0.05 (95 % C.I.).

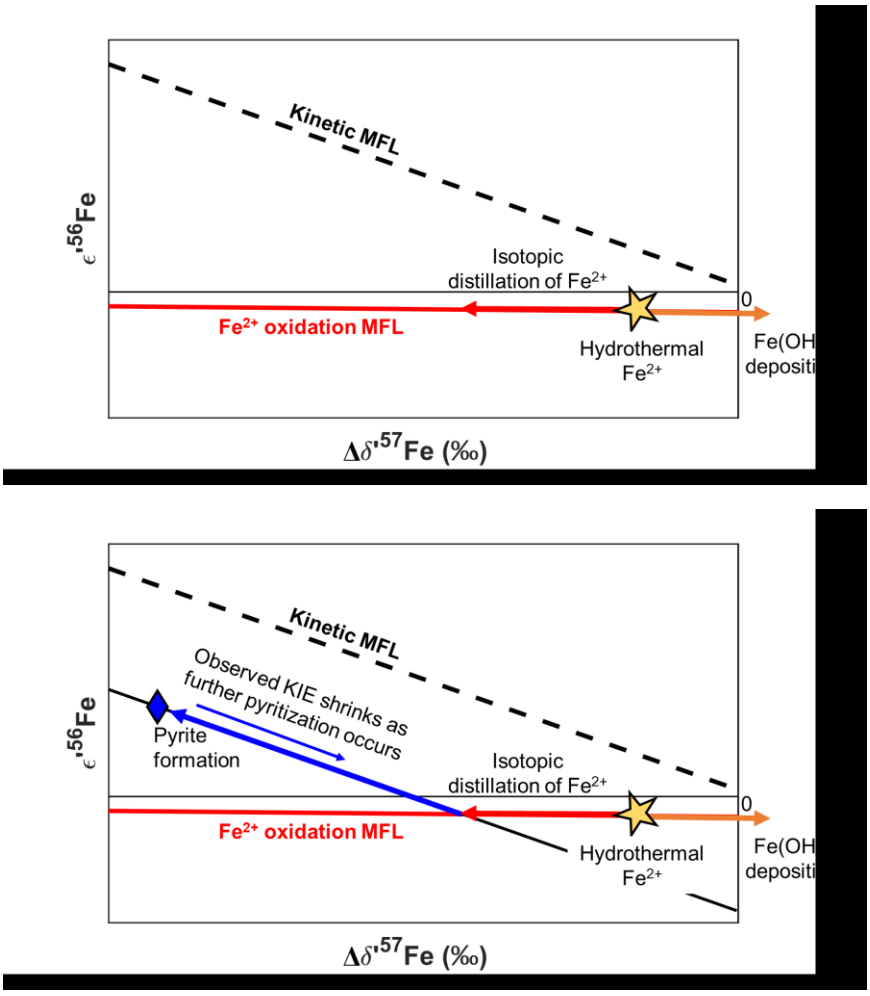

Fig. S5.

Conceptual illustration of the two-step process (Fe^{2+} isotopic distillation by partial oxidation and subsequent partial pyritization) that we propose for generating triple-Fe-isotopic composition of isotopically depleted pre-GOE pyrites, and the procedure for determining Fe-isotopic contributions of pyritization and initial isotopic composition of the pyrite-forming water mass to the Fe-isotopic composition of pyrite. The $\Delta\delta'^{57}$Fe value at where a trajectory for KIE during pyrite precipitation (with slope a_{KIE}) intercepts the oxidative IF MFL ($\Delta\delta'^{57}Fe_w$) is determined by simultaneous solving of two linear equations. The difference between $\Delta\delta'^{57}Fe_w$ and $\Delta\delta'^{57}Fe_{py}$ gives the expression of the KIE during pyritization, which is used to determine the degree of pyritization (f_{py}) of the pre-pyritization water mass, assuming that the pyrite is a cumulative product of all precipitated pyrite. $\Delta\delta'^{57}Fe_w$ is assumed to be the $\Delta\delta'^{57}$Fe value of the pre-pyritization water mass, and its isotopic composition reflects the degree of isotopically heavy Fe^{3+}-oxyhydroxide removal (F_{ox}) that took place prior to the formation of pyrite. $\Delta\delta'^{57}$Fe values are differences from IRMM-014.

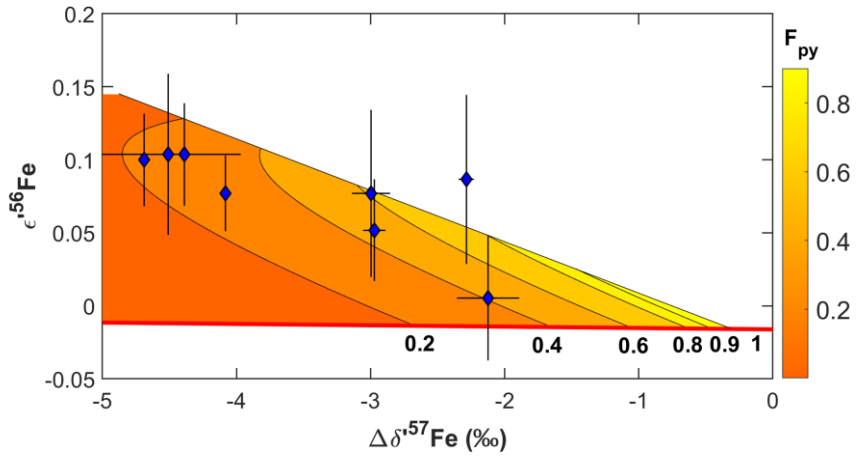

Fig. S6.

Fractional pyrite sink for upwelled Fe (F_{py}) from triple-Fe-isotopic data. F_{py} values are calculated as $F_{py} = f_{py} \times (1 - F_{ox})$. Corresponding f_{py} and F_{ox} contours are plotted in Figure 2C of the main text. $\Delta\delta'^{57}$Fe values are differences from IRMM-014.

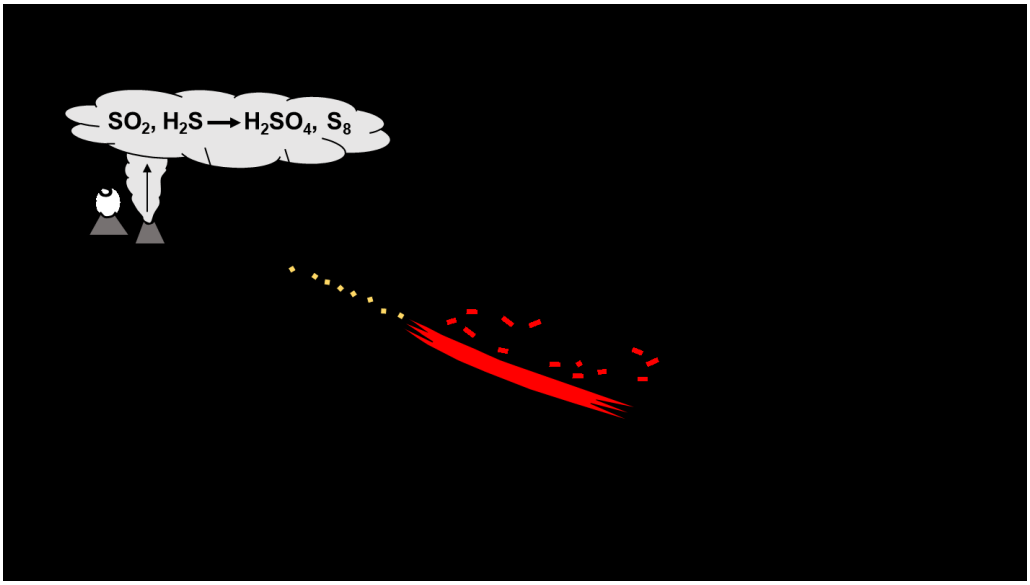

Fig. S7.

Basin cross-section illustrating marine iron cycle before the GOE informed by triple-Fe-isotopic systematics (*9*, *10*, *31*). Dissolved Fe^{2+} in deep-ocean waters fed by hydrothermal vents was upwelled onto continental margins. Oxidation of Fe^{2+} across a spatially diffuse redoxcline led to deposition of Fe^{3+}-oxyhydroxide-rich sediments including IFs. In sedimentary environments with high organic carbon burial, the remaining dissolved Fe^{2+} was incorporated into pyrite, with pyritization before the GOE being limited by sulfur availability controlled by volcanic outgassing.

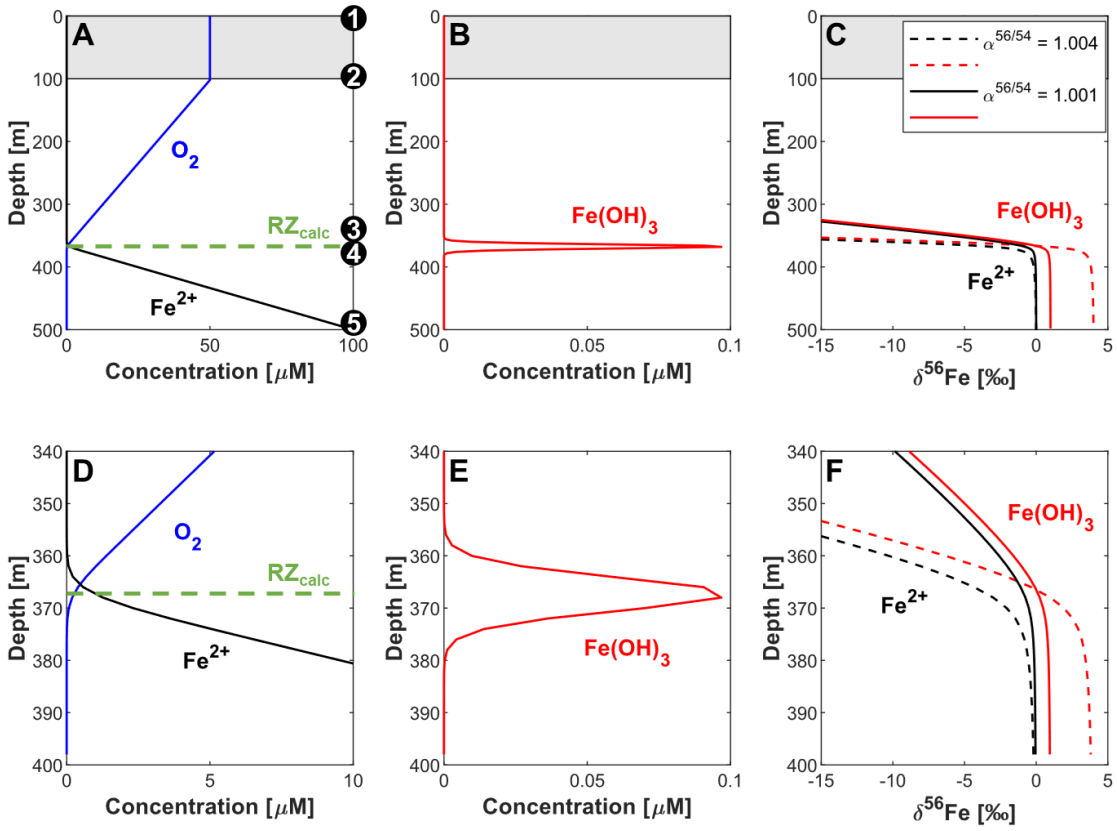

Fig. S8

Depth profiles of outputs from 1-D dispersion-reaction model for Fe^{2+} oxidation (*34*). Input parameters are given in Table S4. A. Depth profiles of O_2 (blue) and Fe^{2+} (black). The green dashed line indicates the position of the reaction zone calculated using a simple scaling argument, and agrees well with the depth in the model output where concentrations O_2 and Fe^{2+} go to zero as $Fe(OH)_3$ concentrations peak. Black circles indicate the layer numbers referred to in Equations S14-S17. B. Depth profile of $Fe(OH)_3$. C. Iron isotopic composition of Fe^{2+} (black) and $Fe(OH)_3$ (red) using two different fractionation factors. D-F. As A-C, zoomed on the depth region surrounding the reaction zone.

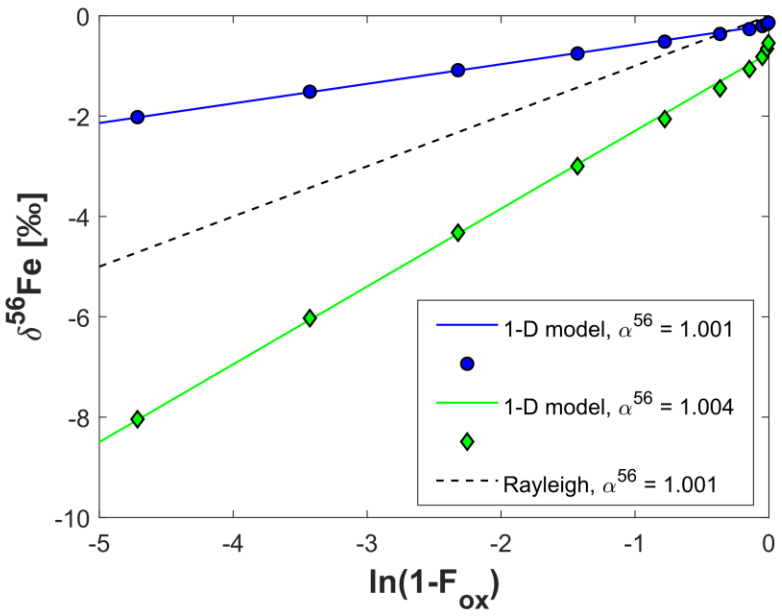

Fig. S9

Evolution of the Fe isotopic composition of Fe^{2+} within the reaction zone of 1-D dispersion-reaction models with different fractionation factors for $Fe(OH)_3$ removal, as a function of F_{ox} (calculated as the $Fe(OH)_3$ formation rate integrated from the base of the model to variable depths, normalized by the total integrated $Fe(OH)_3$ precipitation in the model water column). All arrays show linear relationships between $\delta^{56}Fe$ and $\ln(1-F_{ox})$, in the same manner as a Rayleigh distillation model (dashed black line), but the slopes of these linear relationships are ~0.4 times the slope expected for a Rayleigh distillation model with the same fractionation factor, α^{56}. Small isotopic depletions at negligible values of F_{ox} likely reflect eddy diffusive effects.

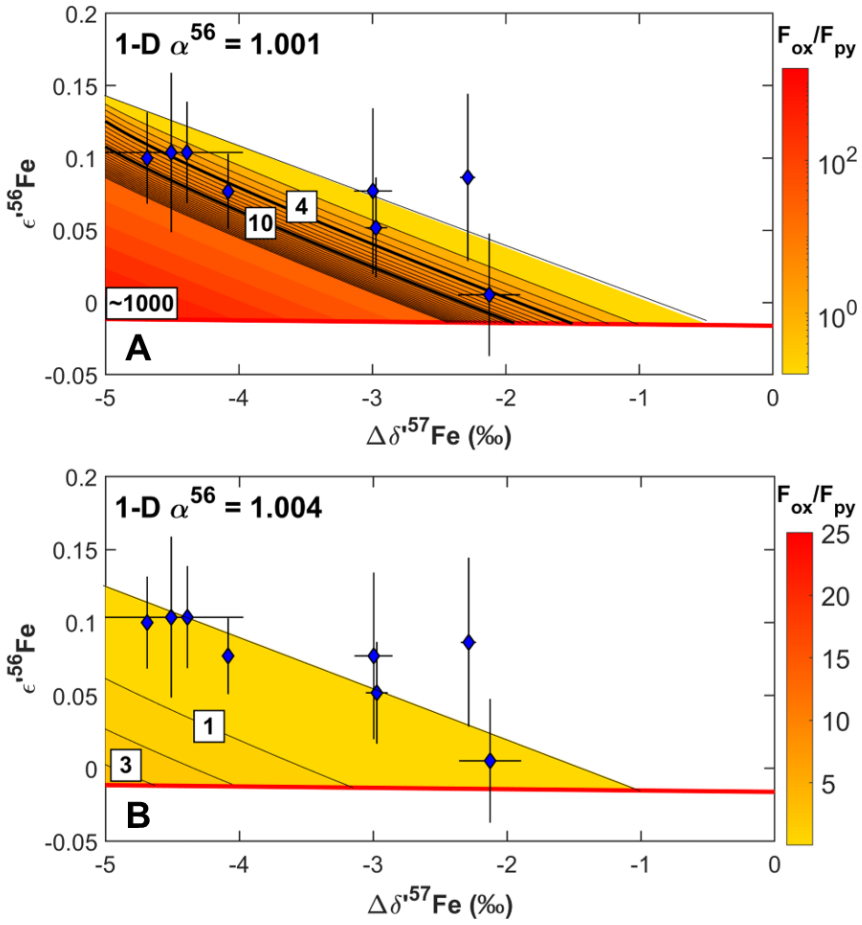

Fig. S10

Pyrite triple-Fe-isotope data and contours of F_{ox}/F_{py} (relative sizes of oxyhydroxide and pyrite sedimentary Fe sinks) calculated using a 1-D dispersion-reaction model for isotopic fractionation during Fe^{2+} oxidation (*34*). Bold contours at 4 and 10 indicate thresholds for net O_2 source *vs.* sink behavior for volcanic H_2S/SO_2 inputs ratios of 1 (*7*) and 0 (*8*), respectively. A. Model using α^{56} = 1.001 for Fe^{2+} oxidation. B. Model using α^{56} = 1.004 for Fe^{2+} oxidation (following the approach of ref. (*34*)). Contours in A are spaced in logarithmic scale. Pyrite triple-Fe-isotopic compositions are consistent with net O_2 sources not being overwhelmed by Fe^{3+} oxyhydroxide formation. $\Delta\delta'^{57}$Fe values are differences from IRMM-014.

Table S1

Triple-Fe-isotope data for Archean-Paleoproterozoic (pre-GOE) pyrites, black shales, and IFs, normalized to exponential (exp) and high-T equilibrium limit (eq) laws

Sample	Age (Ga)	Sample type	$\delta'^{56}Fe$	95% C.I.	$\delta'^{57}Fe$	95% C.I.	$\epsilon'^{56}Fe_{exp}$	$\epsilon'^{56}Fe_{eq}$	95% C.I.	n
EBA-1 1057.5 Py	2.32	pyrite	1.034	0.153	1.527	0.229	0.080	-0.012	0.039	42
EBA 2/30 Py	2.32	pyrite	-2.023	0.095	-2.996	0.143	-0.103	0.077	0.057	12
DO29 14.95 Py	2.5	pyrite	-1.539	0.037	-2.286	0.057	-0.051	0.087	0.058	34
WB-98 520.8 Py	2.52	pyrite	-2.010	0.056	-2.972	0.083	-0.127	0.052	0.035	33
WB-98 519.68 Py	2.52	pyrite	-1.440	0.156	-2.125	0.232	-0.122	0.005	0.042	27
SF-1 599.88 Py	2.65	pyrite	-3.166	0.018	-4.688	0.025	-0.181	0.100	0.032	53
SF-1 623.6 Py	2.65	pyrite	-2.762	0.020	-4.082	0.028	-0.168	0.077	0.026	76
SF-1 642.8 Py	2.65	pyrite	-0.228	0.024	-0.343	0.035	0.029	0.049	0.039	55
FVG-1 752.8 A Py	2.66	pyrite	-3.046	0.367	-4.508	0.540	-0.167	0.104	0.055	21
FVG-1 752.8 B Py	2.66	pyrite	-2.967	0.020	-4.389	0.030	-0.160	0.104	0.035	55
EBA-1 1057.5 BS	2.32	black shale	0.072	0.091	0.105	0.139	-0.004	-0.011	0.042	46
FVG-1 765.8 BS	2.66	black shale	-0.546	0.064	-0.804	0.093	-0.051	0.065	0.059	12
FVG-1 774 BS	2.66	black shale	-1.577	0.123	-2.319	0.172	-0.074	0.008	0.051	29
FVG-1 827.8 BS	2.66	black shale	0.093	0.284	0.136	0.448	0.016	-0.003	0.201	10
REX 167.5	2.40	IF	-1.981	0.115	-2.915	0.168	-0.227	0.014	0.051	12
REX 187.5	2.40	IF	-2.692	0.008	-3.978	0.011	-0.224	-0.052	0.024	109
Hotazel #41	2.40	IF	-2.286	0.021	-3.354	0.032	-0.258	-0.056	0.046	39
RM5	2.47	IF	-0.008	0.276	-0.014	0.412	0.011	0.011	0.082	12
WIT-18-740A	2.48	IF	-1.199	0.067	-1.767	0.090	-0.111	-0.005	0.072	10
ZO4-31	2.70	IF	0.796	0.132	1.169	0.200	0.085	0.015	0.059	26
JD-C165A	2.74	IF	1.624	0.019	2.407	0.028	0.126	-0.019	0.019	184
JD-65-296-1	2.74	IF	1.030	0.265	1.527	0.396	0.002	-0.090	0.052	23
PO5-1	2.95	IF	-1.384	0.028	-2.039	0.039	-0.103	-0.016	0.031	55
PO5-6	2.95	IF	-0.696	0.142	-1.028	0.210	-0.065	0.019	0.074	26
PO5-7	2.95	IF	-1.290	0.224	-1.900	0.336	-0.130	-0.004	0.037	12
IF-G	3.83	IF	0.611	0.012	0.878	0.019	0.052	-0.001	0.030	24

All isotope ratios are reported normalized to IRMM-524, which has an isotopic composition identical to IRMM-014 (*43*). The value of n refers to the total number of standard-sample brackets analyzed. $\delta'^{57}Fe$ and $\epsilon'^{56}Fe$ were determined from the same analyses. δ' values for natural samples are discussed as $\Delta\delta'$ values (differences from IRMM-014) in the text.

Table S2

Triple-Fe-isotopic data for pyrite precipitation experiments, normalized to exponential (exp) and high-T equilibrium limit (eq) laws

Sample	$\delta'^{56}Fe$	$\delta'^{56}Fe-\delta'^{56}Fe_0$	95% C.I.	$\delta'^{57}Fe$	$\delta'^{57}Fe-\delta'^{57}Fe_0$	95% C.I.	n(δ′)	$\epsilon'^{56}Fe_{exp,\ IRMM-524}$	$\epsilon'^{56}Fe_{eq,\ IRMM-524}$	$\epsilon'^{56}Fe_{exp}$	$\epsilon'^{56}Fe_{eq}$	95% C.I.	n(ϵ′)
SB1-4 initial	0.262		0.045	0.371		0.064	5	0.031	0.009			0.020	40
SB5-10 initial	0.236		0.041	0.414		0.081	5	0.027	0.002			0.014	76
SB1 FeS	0.505	0.243	0.045	0.752	0.381	0.064	5	0.080	0.035	0.049	0.027	0.039	21
SB1 Py	-1.939	-2.201	0.045	-2.897	-3.269	0.064	5	-0.039	0.134	-0.070	0.126	0.040	26
SB2 FeS	0.421	0.159	0.045	0.647	0.276	0.064	5	0.028	-0.011	-0.003	-0.020	0.074	10
SB2 Py	-2.320	-2.582	0.045	-3.168	-3.540	0.064	5	-0.061	0.129	-0.092	0.120	0.054	9
SB3 FeS	0.494	0.232	0.045	0.697	0.326	0.064	5	0.040	-0.002	0.009	-0.010	0.053	20
SB3 Py	-1.810	-2.072	0.045	-2.708	-3.080	0.064	5	-0.069	0.093	-0.100	0.084	0.031	17
SB4 FeS	0.564	0.302	0.045	0.818	0.447	0.064	5	0.024	-0.025	-0.007	-0.034	0.049	9
SB4 Py	-1.816	-2.078	0.045	-2.705	-3.077	0.064	5	-0.061	0.101	-0.092	0.092	0.055	10
SB5 FeS	0.353	0.117	0.041	0.547	0.133	0.081	5	0.028	-0.005	0.001	-0.007	0.069	9
SB5 Py	-1.915	-2.151	0.041	-2.885	-3.300	0.081	5	-0.019	0.153	-0.046	0.152	0.021	27
SB6 FeS	0.412	0.176	0.041	0.587	0.173	0.081	5	0.030	-0.005	0.003	-0.007	0.055	9
SB6 Py	-1.777	-2.013	0.041	-2.668	-3.083	0.081	5	-0.049	0.111	-0.076	0.109	0.046	9
SB8 FeS	0.551	0.315	0.041	0.775	0.361	0.081	5	0.046	-0.001	0.019	-0.003	0.043	20
SB8 Py	-1.755	-1.991	0.041	-2.600	-3.016	0.081	5	0.001	0.157	-0.026	0.155	0.023	28
SB9 FeS	0.563	0.327	0.041	0.845	0.431	0.081	5	0.069	0.018	0.042	0.016	0.031	27
SB9 Py	-1.636	-1.873	0.041	-2.415	-2.830	0.081	5	-0.037	0.108	-0.063	0.106	0.060	20
SB10 FeS	0.620	0.384	0.041	0.919	0.505	0.081	5	0.035	-0.020	0.008	-0.022	0.036	29
SB10 Py	-1.693	-1.930	0.041	-2.491	-2.906	0.081	5	-0.062	0.088	-0.088	0.086	0.035	28

δ′ and $\epsilon'^{56}Fe_{IRMM-524}$ values are reported normalized to IRMM-524, which has an isotopic composition identical to IRMM-014 (*43*). $\delta'-\delta'_0$ values are the differences between FeS and pyrite samples and the starting material for the experiments and are equivalent to the Δδ′ values discussed in the text. $\epsilon'^{56}Fe$ is defined in the text based on differences from the starting material, so $\epsilon'^{56}Fe$ values given here and displayed in the figures reflect differences between the $\epsilon'^{56}Fe_{IRMM-524}$ values of the experimental products (FeS: residual FeS, and Py: pyrite precipitate) and the $\epsilon'^{56}Fe_{IRMM-524}$ values of the respective initial batches of starting FeS (used for samples SB1-4, and SB5-10). The values of n(δ′) and n(ϵ′) refer to the total number of standard-sample brackets analyzed for δ′ and ϵ′ measurements, respectively. δ′ and ϵ′ measurements were made separately using different analytical methods, detailed in the text. Starting material for samples SB1-4 and SB5-10 were analyzed 40 and 76 times, respectively.

Table S3

Geological unit and age information for Archean-Paleoproterozoic pyrite, black shales, and IFs

Sample	Geological unit	Age (Ga)	Sample type	Refs.
EBA-1 1057.5 Py	Timeball Hill Fm	2.32	pyrite	(*9*)
EBA 2/30 Py	Timeball Hill Fm	2.32	pyrite	(*9*)
DO29 14.95 Py	Mount McRae Shale	2.50	pyrite	(*9*)
WB-98 520.8 Py	Gamohaan Fm	2.52	pyrite	(*9*)
WB-98 519.68 Py	Gamohaan Fm	2.52	pyrite	(*9*)
SF-1 599.88 Py	Lokammona Fm	2.65	pyrite	(*9*)
SF-1 623.6 Py	Lokammona Fm	2.65	pyrite	(*9*)
SF-1 642.8 Py	Lokammona Fm	2.65	pyrite	(*9*)
FVG-1 752.8 A Py	Jeerinah Fm	2.66	pyrite	(*9*)
FVG-1 752.8 B Py	Jeerinah Fm	2.66	pyrite	(*9*)
EBA-1 1057.5 BS	Timeball Hill Fm	2.32	black shale	(*9*, *30*)
FVG-1 765.8 BS	Jeerinah Fm	2.66	black shale	(*9*, *30*)
FVG-1 774 BS	Jeerinah Fm	2.66	black shale	(*9*, *30*)
FVG-1 827.8 BS	Jeerinah Fm	2.66	black shale	(*9*, *30*)
REX 167.5	Hotazel Fm	2.43	IF	(*2*, *28*, *55*)
REX 187.5	Hotazel Fm	2.43	IF	(*2*, *28*, *55*)
Hotazel #41	Hotazel Fm	2.43	IF	(*2*, *28*, *55*)
RM5	Brockman IF	2.47	IF	(*10*)
WIT-18-740A	Westerburg area IF	2.48	IF	(*10*)
ZO4-31	Manjeri IF	2.70	IF	(*10*)
JD-C165A	Mary River IF	2.74	IF	(*10*)
JD-65-296-1	Mary River IF	2.74	IF	(*10*)
PO5-1	Mozaan Gp	2.95	IF	(*10*)
PO5-6	Mozaan Gp	2.95	IF	(*10*)
PO5-7	Mozaan Gp	2.95	IF	(*10*)
IF-G	Isua Supracrustal Belt	3.83	IF	(*54*, *56*)

Reference numbers refer to Supplementary Reference List in the Supplementary Information

Table S4

Fe-O_2 dispersion-reaction steady-state model parameters

Parameter		Value
Water column depth (m)		500
Eddy diffusion coefficient ($cm^2\ s^{-1}$)		0.1
[O_2] (µmol L^{-1})	Upper (within photic zone)	50
	Lower	No-flux
[Fe^{2+}] (µmol L^{-1})	Upper	No-flux
	Lower	100
Photic zone depth range (m)		0-100
Temperature (°C)		25
Salinity (ppt)		35
$Fe(OH)_3$ settling rate constant (day^{-1})		0.79
Simulation time (yrs)		2000
$\delta^{56}Fe_{Fe2+,initial}$ (‰)		0
$\alpha_{Fe(OH)3\text{-}Fe2+}$		1.001, 1.002, 1.004

Input parameters match those of Czaja *et al*. (2012) (*34*), except the fixed photic-zone [O_2], which matches the value reached at the base of the photic zone in Czaja *et al*. (*34*), for the equivalent model run (run 1 in that study).

Table S5

Estimated fractional size of iron sinks and shelf sedimentary Fe/S ratios for isotopically light pyrites

Sample	Age bin (Ga)	F_{ox}	f_{py}	F_{py}	Moles O_2 yield (per mole FeS_2)	Age-bin average O_2 yield
EBA 2/30	2.32	$0.47^{+0.45}_{-0.42}$	$0.69^{+0.31}_{-0.51}$	$0.43^{+0.18}_{-0.32}$	0.35 (1.06)	0.35 (1.06)
DO29 14.95	2.50-2.52	$0.33^{+0.56}_{-0.25}$	$0.57^{+0.41}_{-0.51}$	$0.58^{+0.19}_{-0.35}$	0.55 (1.51)	0.30 ± 0.21 (0.96 ± 0.47)
WB-98 520.8	2.50-2.52	$0.59^{+0.18}_{-0.54}$	$0.84^{+0.16}_{-0.51}$	$0.36^{+0.26}_{-0.26}$	0.23 (0.80)	0.30 ± 0.21 (0.966 ± 0.47)
WB-98 519.68	2.50-2.52	$0.71^{+0.19}_{-0.59}$	$0.99^{+0.01}_{-0.27}$	$0.29^{+0.44}_{-0.23}$	0.12 (0.56)	0.30 ± 0.21 (0.96 ± 0.47)
SF-1 599.88	2.65-2.66	$0.70^{+0.23}_{-0.60}$	$0.65^{+0.35}_{-0.58}$	$0.18^{+0.04}_{-0.13}$	0.003 (0.31)	0.05 ± 0.02 (0.41 ± 0.05)
SF-1 623.6	2.65-2.66	$0.70^{+0.24}_{-0.60}$	$0.75^{+0.25}_{-0.59}$	$0.23^{+0.10}_{-0.17}$	0.06 (0.42)	0.05 ± 0.02 (0.41 ± 0.05)
FVG-1 752.8 A	2.65-2.66	$0.67^{+0.28}_{-0.59}$	$0.63^{+0.37}_{-0.58}$	$0.21^{+0.04}_{-0.16}$	0.04 (0.39)	0.05 ± 0.02 (0.41 ± 0.05)
FVG-1 752.8 B	2.65-2.66	$0.62^{+0.31}_{-0.55}$	$0.58^{+0.40}_{-0.52}$	$0.24^{+0.03}_{-0.17}$	0.10 (0.51)	0.05 ± 0.02 (0.41 ± 0.05)

For F_{ox}, f_{py}, and F_{py} values, central estimates are 50% percentiles, and uncertainties are 95 % C.I. from Monte Carlo simulations. For O_2 yields, central estimates are calculated from central estimates for F_{ox} and $F_{py\ values}$. The first number assumes volcanic H_2S/SO_2 input ratio of 1 (*7*), second number (in parentheses) assumes volcanic H_2S/SO_2 input ratio of 0 (*8*). Error bars for Age-bin averages are the 95 % C.I. of the average values.